Strongly enhanced visible light photoelectrocatalytic hydrogen evolution reaction in n-doped MoS2 /TiO2(B) heterojunction by selective decoration of platinum nanoparticles at the MoS2 edge sites

Paul, Kamal Kumar; Narayanaru, Sreekanth; Biroju, Ravi Kumar; Pattison, Alexander J; López, Daniel Escalera; Guha, Anku; Tharangattu Narayanan, Narayanan; Rees, Neil Vaughan; Theis, Wolfgang; Giri, P K

DOI:
10.1039/C8TA06783J

Document Version
Peer reviewed version

Citation for published version (Harvard):
Paul, KK, Narayanaru, S, Biroju, RK, Pattison, AJ, López, DE, Guha, A, Tharangattu Narayanan, N, Rees, NV, Theis, W & Giri, PK 2018, 'Strongly enhanced visible light photoelectrocatalytic hydrogen evolution reaction in n-doped MoS_2 /TiO_2(B) heterojunction by selective decoration of platinum nanoparticles at the MoS_2 edge sites', *Journal of Materials Chemistry A*. https://doi.org/10.1039/C8TA06783J

Journal of
Materials Chemistry A

Accepted Manuscript

This article can be cited before page numbers have been issued, to do this please use: K. K. Paul, S. Narayanaru, R. K. Biroju, A. J. Pattison, D. E. López, A. Guha, N. Tharangattu Narayanan, N. V. Rees, W. Theis and P. K. Giri, *J. Mater. Chem. A*, 2018, DOI: 10.1039/C8TA06783J.

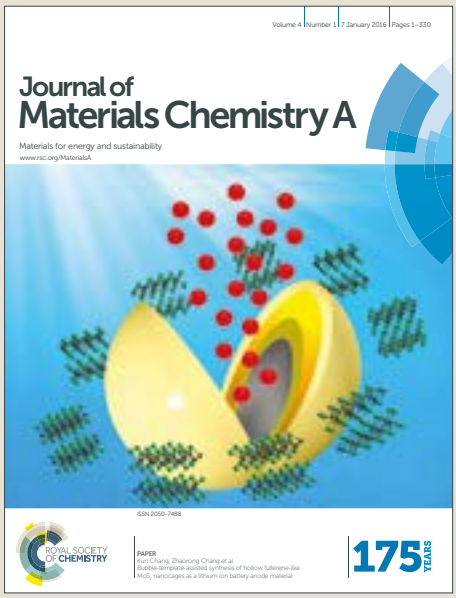

ROYAL SOCIETY OF CHEMISTRY

rsc.li/materials-a

View Article Online
DOI: 10.1039/C8TA06783J

Strongly Enhanced Visible Light Photoelectrocatalytic Hydrogen Evolution Reaction in n-doped MoS_2/TiO_2(B) Heterojunction by Selective Decoration of Platinum Nanoparticles at the MoS_2 Edge Sites

Kamal Kumar Paul[1], N. Sreekanth[2], Ravi K. Biroju[3], Alexander J Pattison[3], Daniel Escalera-López[3,4], Anku Guha[2], Tharangattu N. Narayanan[2], Neil Vaughan Rees[4], Wolfgang Theis[3], and P. K. Giri[1, 5*]

[1]Department of Physics, Indian Institute of Technology Guwahati, Guwahati -781039, India

[2] Tata Institute of Fundamental Research, Sy. No. 36/P, Gopanpally Village, Serilingampally Mandal, Ranga Reddy District, Hyderabad - 500 107, India.

[3]Nanoscale Physics Research Laboratory, School of Physics and Astronomy, University of Birmingham, Birmingham B15 2TT, United Kingdom.

[4]Centre for Hydrogen and Fuel Cell Research, School of Chemical Engineering, University of Birmingham, Edgbaston B15 2TT, Birmingham, United Kingdom.

[5]Centre for Nanotechnology, Indian Institute of Technology Guwahati, Guwahati -781039, India

Abstract

Herein, we demonstrate strongly enhanced visible light photoelectrocatalytic hydrogen evolution reaction (HER) in few-layer MoS_2 grown on a mesoporous TiO_2(B) nanobelt (NB) by selective decoration of platinum (Pt) nanoparticles (NPs) on the edge/defect sites of the MoS_2 layer. Three catalytically active components are anchored together to increase the photoelectrocatalytic HER activity synergistically, beyond that of commercial Pt/C electrodes (20 wt% Pt). An extremely low concentration of Pt NPs (1.4 wt%) with average size ~3.8 nm, were decorated over the preferentially edge-site-exposed few-layer MoS_2, with lateral sizes

* Corresponding author, email: giri@iitg.ernet.in

View Article Online
DOI: 10.1039/C8TA06783J

130-350 nm, as evidenced from the high-angle annular dark-field STEM imaging. During the heterojunction formation, S is doped in the TiO_2 layer causing the high density of electrons in TiO_2 that migrate to the MoS_2 layer inducing n-type doping in it and thus TiO_2 acts as an efficient photocathode in the photoelectrocatalysis. Quantitative XPS analysis reveals that the catalytically active bridging S_2^{2-}/apical S^{2-} increases up to ~72% after the formation of the ternary system (Pt@MoS_2/TiO_2(B). S-enriched MoS_2/TiO_2(B) selectively loaded with Pt NPs on the edge sites of MoS_2 exhibits a giant enhancement in the HER activity in an acidic medium under the light. We record nearly 16 fold higher exchange current density (0.296 mA/cm^2) for the ternary system as compared to the MoS_2/TiO_2 binary system under visible light excitation. The marginal Pt loaded ternary system exhibits an extremely low charge transfer resistance (14Ω) and low overpotential as well as Tafel slope (-74 mV and 30 mV dec^{-1}, respectively) boosting the overall HER performance under the visible light. Chronopotentiometric measurements reveal the high stability of binary and ternary system to sustain a 10 mA/cm^2 cathodic current up to 12 hours. The results show that the marginally-loaded Pt NPs activate the inert basal plane, edge sites of MoS_2 and porous sites of TiO_2, making an integrated network where the photogenerated electrons can easily be injected from the TiO_2 to MoS_2 and then to Pt NPs, presenting a feasible approach to boost the HER activity under visible light.

Keywords: *Pt@MoS_2/TiO_2 heterostructure; Edge controlled MoS_2; n-type doped MoS_2; Photoelectrocatalysis; Hydrogen evolution reaction.*

1. Introduction

The fast-rising energy crisis and environmental pollution is driving the development of new, sustainable, pollution-free sources that can be used on an industrial scale. Hydrogen

View Article Online
DOI: 10.1039/C8TA06783J

is believed to be one of the most promising alternatives to fossil fuels and a source of renewable green energy due to its high energy density and carbon-free combustion emission. Solar-light-driven electrocatalysis using semiconductor TiO_2 and its heterostructures (HSs) is one of the most promising sustainable technologies for the generation of hydrogen by water splitting.[1-7] To make the system commercially viable, the electrocatalyst should be solar light active, efficient and highly stable. To broaden the light harvesting window from UV to visible/NIR and increase the catalytic activity, numerous strategies have been explored, including impurity doping[8-11], staggered-type HSs[12, 13] and TiO_2-based plasmonic HSs with noble metal nanoparticles (NPs)[14-18] etc. In a heterostructured system, the presence of a heterojunction modifies the band positions as well as their inclination at the interface facilitating the migration of photogenerated charge carriers through the heterojunctions, which makes a highly efficient electrocatalyst.[19] Though platinum (Pt) group noble metals are the most efficient conventional electrocatalysts, their extremely high cost and scarcity in nature hinder their industrial-scale usage.[20] Graphene-based two-dimensional (2D) transition metal dichalcogenide nanosheets, especially MoS_2 based heterostructures, have recently received much attention as a noble-metal-free catalyst and an anode material for energy storage device.[21-26] Recently, Pi et al.[27] demonstrated an extraordinary catalytic performance by TiO_2 nanostructure decorated with 1T-MoS_2 nanosheets under solar light. Thus, MoS_2 has now been recognized as an efficient co-catalyst incorporated with TiO_2 nanostructures due to its structural anisotropy, chemical inertness, good electroconductivity, and efficient catalytic properties.[28-30] Theoretical and experimental studies found that the HER ability of MoS_2 mainly derives from the edge sites of its 2D layers, whereas the basal planes are catalytically inert, limiting its overall performance.[31] Thus, tuning the architecture of MoS_2 to preferentially edge-exposed sites, semiconducting (2H) to metallic (1T) phase transformation, introduction of vacancies and incorporation with metal NPs are the

View Article Online
DOI: 10.1039/C8TA06783J

synergistic strategies for the enhancement of HER activity.[32-35] Recently, edge-site-activated ultra-thin MoS_2 nanostructures with optimum defect density, especially S-vacancies, have been identified as tunable active sites to stimulate the originally inert basal plane for the HER.[36, 37] Although these edge sites and defects in the MoS_2 lattice may introduce additional active sites on its basal plane, their incorporation hampers the electron transport properties, leading to low overall HER activity. Zhou et al.[38] and Li et al.[28] have modified the morphology of TiO_2 from ultra-small spherical NPs to long nanobelts (NBs) and employed few-layer MoS_2 nanosheets on them with the high catalytic surface area, which in turn enhanced the hydrogen generation efficiency synergistically. A few groups considered conductive carbon fiber cloths to decorate vertically aligned and preferentially edge-site-exposed MoS_2 nanostructures, which provide very low catalyst-electrode contact resistance, leading to enhanced HER performance.[39, 40] More recently, Xu et al.[4] demonstrated a smart strategy of utilizing the inert basal plane by loading 2.45 wt% of Pt NP on the porous MoS_2 nanostructures anchored vertically with the carbon fiber cloths. It was shown that the loaded Pt NPs could serve both as additional active HER sites and enable fast electron transport, which in turn reduce Pt consumption without compromising the HER activity. It may be noted that though there are several reports on the catalytic activity of binary MoS_2/Pt and TiO_2/Pt system, there is hardly any report on the TiO_2/MoS_2/Pt composite system.[4, 41-43] Very recently, photocatalytic and electrocatalytic H_2 generation in TiO_2/Pt/MoS_2 composite system was reported by Li et al.[44]. However, the system was not well characterized and the performance of the composite system was comparable or inferior to that of binary systems. Unlike the earlier reports, we have chosen a porous TiO_2(B) nanobelt as a novel platform for the growth of edge site exposed few-layer MoS_2. Subsequently, Pt NPs are preferentially decorated at the edge sites of MoS_2 and porous sites of TiO_2(B) with ultralow concentration. To the best of our knowledge, a thorough understanding of such a ternary system and its

View Article Online
DOI: 10.1039/C8TA06783J

visible light PEC activity has not been explored in the literature. In particular, the role of individual components in a ternary system needs to be addressed to exploit its application in next-generation photoelectrocatalysis experiments.

Herein, we carried out a controlled growth of porous TiO_2(B) NBs (TB) via a solvothermal method and its in-situ surface decoration with discrete few-layer MoS_2 by a second stage hydrothermal treatment. Incorporation of a marginal amount of Pt NP as a suitable co-catalyst on the surface of MoS_2/TiO_2(B) (MSTB) can generate additional surface active sites, increasing the overall conductivity and charge separation through the multiple heterojunctions. The ternary catalyst contains the maximum amount of bridging S_2^{2-}/apical S^{2-} which are known to be catalytically active. As the Pt NPs are decorated on the edge/porous sites of the MoS_2/TiO_2 HS (PMSTB), the photoexcited electrons can easily be transferred from TiO_2 to Pt sites directly as well as via the MoS_2 edge-sites, leading to a remarkable enhancement in the exchange current density (j_0) and thus HER activity compared to dark conditions that is much higher than the pristine or the other HSs. Thus, a rational design of hierarchical nanostructures with a marginal amount of Pt loading (1.4 wt%) is crucial for achieving superior photoelectrocatalytic systems.

2. Experimental procedure

2.1. Preparation of TiO_2 NBs

Anatase TiO_2 nanopowder, ethylene glycol, and sodium hydroxide (NaOH) pellets were used in our experiments as received from Merck without any further purification. In a typical synthesis, 0.2 g of anatase TiO_2 powder (average particle size ~ 80 nm) was mixed vigorously in a 50 ml aqueous NaOH solution (10 M) with an equal volume of ethylene glycol. Next, the mixed white solution was transferred into a Teflon-lined autoclave (Berghof, BR-100) and the solution temperature was maintained at 220 °C monitored with a

View Article Online
DOI: 10.1039/C8TA06783J

thermocouple inserted into the Teflon chamber for 16 hr with a constant magnetic stirring at 500 rpm. The resultant precipitates were washed thoroughly with DI water and 0.1 N HCl to reduce its pH to 7, which ensures the full exchange of Na^+ by H^+ ions. Then, the obtained H-titanate NBs were calcined at 500 °C for 5 h in air to get porous TiO_2(B) NBs.

2.2. Growth of MoS_2/TiO_2 NBs heterostructures

Typically, 20 mg of TiO_2(B) NBs powder was homogeneously dispersed into 40 ml of Milli-Q water in a bath sonication for 30 min. Next, 60 mg sodium molybdate ($Na_2MoO_4 \cdot 2H_2O$) and 120 mg thioacetamide (C_2H_5NS) as a source of Mo and S, respectively were dissolved in the above dispersion.[45] The mixture was then treated in a Teflon-lined stainless steel autoclave at 240 °C for 24 h with a constant magnetic stirring at 250 rpm. The resultant black precipitate was washed thoroughly with DI water to eliminate the additional salts and impurities followed by a centrifugation. A uniform decoration of few-layer MoS_2 on the TiO_2 NBs platform with 1:1 weight of MoS_2 and TiO_2 was obtained after a drying process at 50 °C for 12 h. For comparison, pure few-layer MoS_2 were synthesized under identical conditions but in the absence of TiO_2 NB platform.

2.3. Decoration of Pt NP on the TiO_2 NBs and MoS_2/TiO_2 NBs heterostructures

50 mg of MoS_2/TiO_2 powder was dispersed into 100 ml of MQ water in an ultrasonic bath for 30 min. 52 mg H_2PtCl_6 was dissolved into 100 ml of MQ water and added drop-wise into the MoS_2/TiO_2 dispersion under magnetic stirring. Then, 50 ml of 0.01 M aqueous $NaBH_4$ solution was added slowly into the above mixture to deposit Pt NP uniformly over the TiO_2 as well as MoS_2/TiO_2 HSs.

2.4. Characterization techniques

View Article Online
DOI: 10.1039/C8TA06783J

The crystal structure of the as-grown catalysts was studied using an X-ray powder diffractometer (XRD) pattern (Rigaku RINT 2500 TTRAX-III, Cu kα radiation). Crystallinity and phase composition of the as-synthesized NRs and the number of layers in MoS_2 have been confirmed by the micro-Raman measurement (LabRam HR800, Jobin Yvon). Morphology and size of the as-synthesized TiO_2 NBs and MoS_2 layer on the TiO_2 NBs have been studied by a field emission scanning electron microscope (FESEM) (Sigma, Zeiss). The high-magnification surface morphologies and structures of the as-grown samples have been studied by a field emission transmission electron microscope (FETEM) (JEOL-JEM 2100F operated at 200 kV). Elemental mapping of various samples was recorded by the FETEM equipped with an energy dispersive X-ray (EDX) spectrometer. Samples for TEM analysis have been prepared on a carbon-coated Cu grid of 400 mesh size (Pacific Grid, USA). In particular, edge sites of MoS_2 layers and the selective decoration Pt NPs were identified using bright field scanning transmission electron microscopy (STEM) mode using an aberration-corrected STEM (JEM 2100F, 200 kV) and corresponding energy-dispersive X-ray spectroscopy (EDS) hypermaps were recorded to analyze the local environment of S, Mo, Pt in TiO_2-based MoS_2 nanoflower and Pt NP modified nanostructures. UV-Vis diffuse reflectance spectroscopy (DRS) measurements were recorded using a commercial spectrophotometer (SHIMADZU 2600). Room temperature steady state PL spectra of the catalysts were recorded with the help of a spectrometer (focal length: 15 cm; blaze wavelength: 500 nm; groove density: 150g mm^{-1}) equipped with a cooled charge-coupled device (Princeton Instruments, PIXIS 100B) detector using a 405 nm diode laser (Coherent, Cube) excitation. X-ray photoelectron spectroscopy (XPS) has been carried out using a PHI X-tool automated photoelectron spectrometer (ULVAC-PHI, Japan) with an Al Kα X-ray beam (1486.6 eV) at a beam current of 20 mA. The shift in the binding

View Article Online
DOI: 10.1039/C8TA06783J

energy of various catalysts has been corrected using the C1s spectrum at 284.8 eV as a standard value.[12]

2.5. Photoelectrocatalysis measurements under visible light

Photoelectrochemical measurements were performed systematically in a conventional three-electrode electrochemical cell: a commercial Ag/AgCl (saturated KCl) (CH instruments) as reference electrode, Pt wire or graphite rod as counter electrode and the as-grown catalysts supported on a glassy carbon substrates were used as working electrodes. Prior to catalyst loading, the surface of the glassy carbon substrate is polished with 50 μm alumina powders on a polishing cloth and washed with DI water. A 4 mg catalyst was dissolved in 1 mL DI water and the dispersion was sonicated for 1 h. A 6 μL of as-prepared sample was drop cast on the glassy carbon electrode (diameter = 3 mm) and dried in the inert atmosphere. The net loading of each catalyst is ~0.34 mg/cm^2. Electrochemical surface area (ECSA) of each catalyst was measured using Randel-sevick equation:

$$I_p = (2.69 \times 105)n^{3/2}AD^{1/2}v^{1/2}C \ ,$$

Where I_p is anodic peak current (amperes), υ is the scan rate of potential, n is the number of electrons involved in the reaction, A is the active surface area (cm^2), C (moles/cm) is the concentration of electroactive species, D is diffusion coefficient (cm^2/s). Thus, the active surface area 'A' of the electrode is calculated from the cyclic voltammetry (CV) response of 5 mM $[Fe(CN)_6]^{3-/4-}$ in 0.1 M KCl at different scan rates. The calculated ECSA for the TB, MS, PMS, PTB, MSTB and PMSTB are 0.038, 0.042, 0.048, 0.050, 0.052 and 0.045 cm^2, respectively.

The photo-electrocatalytic studies were performed using a Bio-Logic SP-300 electrochemical workstation. A 250 W Xenon lamp (Lelesil Innovative Systems, India) was used as the visible light source with wavelength range ~370–730 nm during the

View Article Online
DOI: 10.1039/C8TA06783J

photoelectrochemical measurements. A 0.5M H_2SO_4 solution was used as an electrolyte, deaerated by N_2 purging until saturation prior to any electrochemical experiment. Linear sweep voltammetry (LSV) was conducted at a scan rate of 5 mV/s. Electrochemical impedance spectroscopy (EIS) was also performed in 0.5M H_2SO_4 under dark and light at HER onset potential of each catalyst over the frequency range 7 MHz–100 Hz with an input sine wave having 10 mV amplitude.

3. Results and discussion

3.1. Morphology studies

Fig. 1(a) shows a FESEM image of pristine TiO_2 NBs with diameter ~30-100 nm and length ~ a few μm, while Fig. 1(b) shows a uniform decoration of Pt NP over the TiO_2 NBs. During the 2nd stage hydrothermal treatment, self-assembly of few-layer MoS_2 nanosheets on the porous TiO_2 NB template transforms it into discrete MoS_2 nanoflowers (NFs) decorated on the TiO_2 NBs with the size distribution 130-350 nm, as shown in Fig. 1(c). Fig. 1(d) shows the FESEM micrograph of Pt NP-decorated MSTB HSs. Large Pt NPs can be observed on the TiO_2 surface may be due to the aggregation. Note that, the deposited Pt NPs on the edge-exposed MoS_2 NFs have appreciably small size and a narrow size distribution (discussed later), and hence the NPs were not discernable here due to the resolution limit of FESEM.

Fig. 2(a,b) exhibit TEM micrographs of Pt NPs decorated on TiO_2 NBs (PTB HS) at two different magnifications, demonstrating an overall uniform decoration of Pt NPs, and the Fig. 2(c) shows an HRTEM lattice fringe pattern of well-crystalline Pt NPs and TiO_2 NBs in PTB. The calculated lattice spacing of 0.22 nm corresponds to the (111) plane of Pt NP, and 0.29 nm and 0.32 nm correspond to the (111) and (002) crystal planes of TiO_2(B), respectively, in the PTB HSs. TEM images in Fig. 2(d,e) reveal the in-situ growth of MoS_2

View Article Online
DOI: 10.1039/C8TA06783J

layers on the porous TiO_2 NBs platform with a broad size distribution of 100-380 nm, which is in good agreement with the FESEM analysis. As evident from the image, the pure MoS_2 crystals with maximally exposed edge active sites appear to be layered wavy petals, and they gather together to form distinct nanorose-like structures on the porous TiO_2 NBs platform due to the high autogenous pressure (~45 bar) inside the autoclave. Insets in Fig 2(d,e) depict the hexagonal diffraction spots and a honeycomb atom arrangement in a 2H-MoS_2, respectively, grown over TB. Fig. S1(a,b) (Supporting Information) reveal the bright field STEM images of MSTB with different magnifications, showing the few-layer growth of MoS_2 over the porous structure of TiO_2 NBs.[46] The HRTEM lattice fringe pattern of MSTB HS shown in Fig. 2(f) clearly reveals the co-existence of few-layer MoS_2 with the TiO_2 lattice. Fig. 2(f) shows a typically layered nanosheet having ~6 sandwiched S–Mo–S layers with interlayer spacing ~0.67 nm. Additional ordered domains with a lattice spacing of 0.28 nm can be assigned to the (100) plane at the basal surface of 2H-MoS_2. The lattice spacing of 0.37 nm, 0.39 nm, and 0.64 nm corresponds to the (110), (201) and (001) crystal planes, respectively for pure B-phase TiO_2. It can be observed from the DF-STEM image of PMSTB shown in Fig. 2(g) that the Pt NPs are selectively decorated at the exposed edge sites of MoS_2 over the MSTB HS and the inset shows the size distribution of Pt NPs over the MSTB HSs. It shows a very narrow size distribution (distribution width ~0.19 nm) with an average size of 3.8 nm. Fig. 2(h,i) depict the dark field and bright field STEM images of Pt NPs anchored selectively on edge/defect sites of MoS_2 layer supported on the TiO_2 NBs, respectively.

In order to estimate the individual contribution of Pt NP and MoS_2 on HER under dark and light conditions, we performed STEM-EDS elemental mappings on the MSTB HSs before and after the modification with Pt NPs. Fig. 3(a) shows a STEM image of PMSTB on which elemental mapping was performed. The EDS elemental mapping reveals that the core of the HS is composed of Ti and O elements, as shown in Fig. 3(b, c), which further confirms

View Article Online
DOI: 10.1039/C8TA06783J

the uniform growth of TiO_2. Fig. 3(d,e) exhibit the elemental mapping for Mo and S, respectively, which supports our argument that the discrete MoS_2 NF grows on the TiO_2 platform as an outer layer. The Pt NPs are observed to be dispersed with overall uniformity over the MoS_2 NFs as confirmed by the elemental map of Pt shown in Fig. 3(f). Similar results of the elemental distribution of Ti, O as the core layer and Mo, S as an outer layer were observed in case of MSTB, as shown in Fig. S2(a-f) (Supporting Information). EDS spectra corresponding to MSTB and PMSTB shown in Fig. S2(g,h) (Supporting Information) confirmed that the ratio of S and Mo is found to be similar before and after Pt loading on to the MSTB HS (see Fig. S2(g,h), Supporting Information). It is clear that the majority of the Pt NPs is embedded at the edge sites of the 2H phase MoS_2 layers. The weight % of S is found to be high indicating S-rich MoS_2 layers in all the catalysts MS to MSTB to PMSTB, as evident from the EDS analysis of pristine samples (see Fig. S3, Supporting Information) which is reported to be superior for the enhanced HER activity.[22] However, in the case of PTB, most of the Pt NPs are preferentially attached to the porous sites of TiO_2 nanostructures.

3.2. Structural analysis

3.2.1. XRD analysis

Fig. S4 (Supporting Information) depicts the XRD pattern of the as-grown catalysts. The diffraction peaks for pristine MoS_2 (marked with "*") in Fig. S4(a) (Supporting Information) detected at $2\theta \approx 14.5°$, 32.9° and 56.5° can be attributed to the (002), (100) and (106) crystal planes, respectively (JCPDS card no. 37-1492). XRD peaks corresponding to pristine TiO_2 NBs (labeled with "♦" mark) match with the standard values of the TiO_2 monoclinic structure.[12] Fig. S4(c) (Supporting Information) shows the diffraction pattern of few-layer MoS_2 designed on porous TiO_2 NBs (MSTB). It can be noted that the diffraction

View Article Online
DOI: 10.1039/C8TA06783J

peak of pristine MoS_2 at ~ 14.5° corresponding to the c-plane was not detected in the case of MSTB. Thus, the absence of this peak confirms the coating of TiO_2 NBs with extremely thin few-layer MoS_2 nanosheets, which may prevent the crystal growth along the c–axis. Fig. S4(d) (Supporting Information) shows the XRD pattern of PMSTB, which clearly confirms the co-existence of Pt, MoS_2, and TiO_2(B) crystals. In the figure, the Pt has been labeled as circles (filled). The diffraction peaks of Pt are relatively sharp, clearly implying its highly crystalline nature.

3.2.2. Raman analysis

In order to investigate the crystallinity, phase and layer numbers in as-grown catalysts, micro-Raman analysis has been conducted, as shown in Fig. 4. Each of the phonon modes of TiO_2 NBs correspond to the monoclinic structure of B-phase TiO_2, see Fig. 4(a). The pristine MoS_2 exhibits two active Raman modes attributed to E_{2g}^1 and A_{1g} having separation of 25.1 cm^{-1}, as shown in Fig. 4(a). However, MSTB exhibits a combination of B-phase TiO_2 and MoS_2. In MSTB, these Raman modes are observed with a reduced separation of 22.3 cm^{-1}, as clarified by the vertical dotted lines. After loading the Pt NPs on MSTB, the intensity of the characteristic MoS_2 peaks is significantly reduced, while that of TiO_2 is not affected much. This may be due to the screening effect of Pt NPs decorated over the edge-rich MoS_2 NFs. Fig. 4(b) exhibits the B_g and A_g Raman modes for B-phase TiO_2 in the pristine TB, MSTB, and PMSTB, and their corresponding Lorentz fittings. It is evident that the intensity of TiO_2 Raman modes decreases after the decoration of MoS_2, which may be due to the bonding of MoS_2 at the porous site of TiO_2 NBs. The B_g and A_g Raman modes of TiO_2 NBs at 123.1 cm^{-1} and 146.7 cm^{-1}, respectively, are broadened and blue shifted after the MoS_2 growth, as shown in Fig. 4(b). The MSTB shows a blue shift of 3.2 cm^{-1} in B_g mode with broadening in FWHM from 10.8 cm^{-1} to 12.9 cm^{-1}. Similarly, for A_g mode, the MSTB HS exhibits a huge blue shift of 6.8 cm^{-1} with an increment in the FWHM from

View Article Online
DOI: 10.1039/C8TA06783J

11.7 cm^{-1} to 22.4 cm^{-1}. Such a large blue shift and broadening are mostly due to a surface strain (compressive type) induced by the MoS_2 nanosheets covered on the TiO_2 surface originating from the non-stoichiometric oxygen vacancy (O_v) defects resulting possibly from the S-doping at the O-site in the TiO_2 lattice.[14, 47, 48] After the loading of Pt NPs over MSTB, no further increase of defect concentration in the TiO_2 lattice is observed. Fig. 4(c) exhibits the E_{2g} and A_{1g} Raman modes for MoS_2 in the pristine MS, MSTB, and PMSTB, and the corresponding Lorentz fittings are also shown. The pristine MoS_2 exhibits two active Raman modes centered at 379.7 cm^{-1} and 404.8 cm^{-1}, which are attributed to $E_{2g}{}^1$ and A_{1g} modes, respectively, as shown in Fig. 4(c). However, in MSTB, these Raman modes are observed at 380.1 cm^{-1} and 402.4 cm^{-1}, respectively.[28, 49] The former peak ($E_{2g}{}^1$) is attributed to the in-plane vibrations and the later one (A_{1g}) to the vertical-plane vibrations in the Mo-S bond of MoS_2 and the separation between these two peaks is mainly determined by the layer number in MoS_2 nanosheets.[50] The estimated frequency differences between these two modes are $\Delta\nu \approx 25.1$ cm^{-1} and 22.3 cm^{-1} for pristine MS and MSTB, respectively. Thus, the growth of few-layer pristine MoS_2 is confirmed and the reduction in $\Delta\nu$ for MSTB may be interpreted as follows: first, the overall growth of layered MoS_2 on the TiO_2 platform leads to a reduced number of layers (bilayer/few-layer): this is due to the presence of numerous porous nucleation sites in TiO_2 NBs which not only act as the nucleation sites for the growth of layered MoS_2, but also constrain their aggregation to yield bilayer/few-layered structures. In contrast, the bare MoS_2 NFs aggregate during the hydrothermal growth due to the absence of any anchoring support, resulting in multilayered MoS_2. Second, in MSTB, the only A_{1g} peak is observed to be redshifted (by ~2.4 cm^{-1}), whereas the E_{2g} peak remained unchanged. This may be due to the softening of A_{1g} vibrations at high electron concentrations, which results from the n-type doping in MoS_2 grown in the vicinity of S-doped and O_V enriched TiO_2.[51, 52] In PMSTB, A_{1g} mode exhibits a further redshift of 1 cm^{-1} with a larger FWHM, indicating

View Article Online
DOI: 10.1039/C8TA06783J

the n-doping effect in MoS_2 lattice. This can be understood from the band bending at the interfaces of MoS_2 and TiO_2, facilitating the electron transfer from the TiO_2 to MoS_2 side, which will be discussed later.

3.2.3. XPS analysis

The chemical valence state, the stoichiometric ratio of the systems and the surface defects present in pristine catalysts and their HS were investigated by the XPS analysis. The Ti 2p core level XPS spectra of pristine TB, were deconvoluted by Gaussian fitting to determine the double peak features of Ti $2p_{3/2}$ and Ti $2p_{1/2}$, as shown in Fig. S5(a) (Supporting Information). The fitted peaks corresponding to the binding energies of 458.8 and 464.5 eV can be attributed to Ti^{4+} cation. Two additional Gaussian peaks centered at 456.7 eV and 461.0 eV related to Ti^{+3} valence states were detected with relative percentage of 4.9% for TB, which reveals the presence of nonstoichiometric O_v defects in the system.[12] Fig. S5(b) (Supporting Information) shows the Pt 4f core level XPS spectrum for the PMSTB, which can be deconvoluted into four symmetric Gaussian peaks, corresponding to the two different valence states of Pt. The Pt $4f_{7/2}$ and Pt $4f_{5/2}$ peaks detected at 71.5 eV and 74.8 eV, respectively, originate from metallic Pt^0, while the other pair of at 72.7 and 76.4 eV correspond to Pt $4f_{7/2}$ and Pt $4f_{5/2}$ of Pt^{2+}, respectively.[53, 54] The area under each peak reveals the relative atomic percentage of Pt^0 and Pt^{2+} as 75.8% and 24.2%, respectively, in PMSTB, signifying that the Pt is mainly in the metallic state. The additional Pt^{2+} in the HS sample may form Pt–O bond due to the chemisorption of oxygen and hydroxyl group on the surface of the Pt NP and MoS_2 layers. Fig. S5(c,d) (Supporting Information) depicts the Mo 3d core-level XPS spectra of MSTB and PMSTB, respectively. The strongest Mo 3d doublet peaks for MSTB detected at 229.2 eV ($3d_{5/2}$) and 232.5 eV ($3d_{3/2}$) shown in Fig. S5(c) correspond to the 4+ oxidation state of Mo, confirming the formation of MoS_2. The shoulder peaks

View Article Online
DOI: 10.1039/C8TA06783J

detected at 226.4 eV and 235.7 eV can be attributed to the S 2s state and Mo 6+ oxidation state, probably due to the formation of MoO_3 during the hydrothermal growth and post-synthesis exposure to air. After the Pt NP decoration on MSTB, the major Mo 3d doublet peaks corresponding to 4+ valence state have been detected at 229.7 eV ($3d_{5/2}$) and 232.9 eV ($3d_{1/2}$). Each of the peak shifts by ~ 0.5 eV towards the higher binding energy side, which may be due to the distortion in the mixed state Mo arising from the generation of oxygen deficiencies in the system as evident from the absence of Mo^{6+} oxidation state.

To characterize the nature of S atoms present in the catalysts, which are responsible for their HER activity, the core level XPS spectra of S were recorded and results are shown in Fig. 5 and the corresponding area percentage is shown in Table 1. The pristine MoS_2 layers contain S atoms with electron binding energies at ~161.9/163.1 eV and ~163.4/164.6 eV, respectively (two sets of doublets), as shown in Fig. 5(a). The lower binding energy doublets are assigned to unsaturated S^{2-} and terminal S_2^{2-}, while the higher binding energy doublets are assigned to bridging S_2^{2-} and apical S^{2-}.[55] In addition to the formation of MoS_2, presence of S^{2-} in the HS sample may correspond to the Ti–S bond formed during the substitution of O-atoms by S-atoms in the TiO_2 crystal lattice, resulting in S-doped TiO_2, which is consistent with the large blue shift in TiO_2 Raman spectra and enhancement of O_V concentration in TiO_2 lattice after the in-situ growth of MoS_2 over TiO_2 (discussed later).[47, 48] Ting et al.[55] demonstrated that the catalytic reactivity, as well as the turnover frequency of hydrogen production, increases almost linearly with increasing the amount of bridging S_2^{2-}/apical S^{2-} in the catalysts. In the present case, pristine MS exhibits S atoms with bridging S_2^{2-}/apical S^{2-} as 39.1% which is found to be increased to 54.4%, after its growth on porous TB, as shown in Fig. 5(a,b). Therefore, the TB NBs not only facilitate the few-layer growth of MoS_2 with edge-exposed sites but also serve as an effective platform for mediating the evolution of MoS_2 with more bridging S_2^{2-}/apical S^{2-} to promote the enhanced

View Article Online
DOI: 10.1039/C8TA06783J

HER activity. It is noteworthy that after Pt NP decoration on MSTB, the bridging S_2^{2-}/apical S^{2-} increases dramatically to 72.2%, as shown in Fig. 5(c). Thus, it is clear that the Pt NP plays a crucial role to increase the bridging S_2^{2-}/apical S^{2-} amount in the HS and eventually in the superior HER performance.[55]

Fig. 6(a-d) displays the O 1s XPS spectra of TB, MSTB, PTB and PMSTB, respectively. The spectra corresponding to pristine TB and PTB possess a long tail towards the higher-energy region making the spectra asymmetric in nature. In addition, MSTB and PMSTB exhibit exceptionally-broad O 1s spectra implying the presence of defects or impurity on its surface. Each O 1s spectra can be fitted with three symmetric Gaussian peaks, as reported in the literature.[56] The first peak at ~530.1 eV is attributed to the TiO_2 crystal lattice and its relative percentages are calculated to be 66.6%, 61.4%, 21.2% and 21.3% for TB, PTB, MSTB, and PMSTB, respectively. Thus, it is clear that the relative percentage of lattice oxygen in TiO_2 decreases marginally after the Pt decoration, but it decreases dramatically after the decoration of MoS_2. The second peak at ~531.2 eV can be assigned to the Ti-O bond ($O_{Ti^{3+}}$) and the relative $O_{Ti^{3+}}$% calculated from the O 1s XPS spectra is tabulated in Table 1. After the decoration of MoS_2, the O_v concentration in the TiO_2 lattice is observed to be more than doubled from 21.1% to 46.1%, which may be due to the substitution of O-atoms in TiO_2 with the S-atoms during the in-situ growth of MoS_2 over TiO_2 platform. This is consistent with the large blue shift in the Raman spectrum. Loading of Pt NPs on TB or MSTB results in the decrease in O_v concentration from its initial value, perhaps due to the presence of Pt^{2+} species, which reduce the vacancy concentration. The third peak at ~532.7 eV is attributed to the hydroxyl group adsorbed on the HS surfaces and its relative percentages are shown in Table 1. Thus, it is observed that introduction of Pt NP in the nanostructures enhances the relative percentage of the adsorbed hydroxyl group from 12.3% to 23.1% for pristine TB and from 32.7% to 47.3% for MSTB. Thus, it can be

View Article Online
DOI: 10.1039/C8TA06783J

concluded that the Pt NP introduces the hygroscopic nature in the nanostructure and also increases the adsorption capability in the system. These exceptionally high defect states may serve as shallow donors and enhance the charge transfer at the multiple interfaces, which in turn improves the overall photoelectrocatalytic water splitting under solar light, as discussed later.

3.3. UV-Vis absorption and photoluminescence study

To investigate the solar energy harvesting efficiency, the pristine and the HS catalysts were analyzed by UV-visible diffuse reflectance spectroscopy (DRS). Fig. 7(a) shows the Kubelka-Munk (K-M) function, F(R), for each of the samples corresponding to their DRS spectra. The pure TiO_2(B) NBs exhibit a sharp rise in absorption (edge) at ~360 nm (indirect bandgap estimated from Tauc plot is ~3.25 eV), which is attributed to its intrinsic band gap absorption. Pristine few-layer MoS_2 NFs exhibit a broad absorption band having a peak at ~670 nm (direct bandgap estimated from Tauc plot ~1.63 eV) showing a large blue shift compared to its bulk counterpart. This may be attributed to the strong quantum confinement effect of the thin and layered MoS_2 nanosheets, which makes the MoS_2 a promising candidate for the visible light photocatalysis.[57] Incorporation of few-layer MoS_2 on TiO_2 NBs enhances the absorption intensity significantly over the wide range of UV-visible-IR range, as shown in Fig. 7(a). Introduction of Pt NPs on the TiO_2 NBs further enhances the visible light absorption efficiency, with a new absorption band centered at ~415 nm, besides its enhanced UV and visible-NIR absorption. Cueto et al.[58] have shown that the Pt NPs with size 5-35 nm exhibit a plasmonic absorption covering a narrow band in the range 200−320 nm, and a broader band with a tail extending up to the NIR region. However, in the case of large Pt NPs the absorption band becomes intense and broad enough as a consequence of stronger plasmonic excitation due to the formation of numerous hotspots between two or more Pt NPs close to each other. In the present work, the Pt NPs decorated over the MoS_2

View Article Online
DOI: 10.1039/C8TA06783J

NFs are closely spaced, which enables high plasmonic excitation generated in the numerous hotspots, and results in high absorption. Interestingly, the absorption edge of the TiO_2 NBs is observed to be red shifted after decoration of MoS_2 NFs as well as Pt NPs. With Pt NPs, the absorption edge of the TiO_2 is red shifted to ~380 nm from ~360 nm. In case of MSTB, it is further redshifted to ~402 nm, which implies an efficient band bending at the interface arising from the strong coupling between the porous TiO_2 and wrapped MoS_2 layers. S-doping in TiO_2 lattice may also be attributed to this red shift.[47] However, maximum red shift is observed in PMSTB (~471 nm), which may be attributed to the strong coupling between each pair of the components MoS_2-Pt, MoS_2-TiO_2, and Pt-TiO_2. Thus, the HSs are expected to be extremely sensitive to the visible-NIR light and would be beneficial for the efficient visible light photoelectrocatalytic hydrogen evolution.

Fig. 7(b) shows a comparison of room temperature PL spectra of TB, MSTB, and PMSTB. Pristine TiO_2 NBs exhibit very weak and broad PL emission having an emission peak at ~515 nm, which is attributed to the single electron trapped oxygen vacancy (O_V) defects (F^+ center) [56, 59]. After the growth of the MoS_2 layer on TiO_2 NB, the PL intensity corresponding to the F^+ center increases strongly, indicating an increase in the concentration of O_V defects. During the in-situ hydrothermal growth of MoS_2 on TiO_2, S-atoms may diffuse and substitute the O-atoms in TiO_2 lattice, causing S-doping in TiO_2. This causes an increase in the O_V concentration and eventual increase in electron density in TiO_2. Due to the high optical absorption and O_V defects in MSTB HS, the PL intensity corresponding to the F^+ center increases substantially. After loading of Pt NPs over MSTB, the PL intensity reduces, which is due to the fast interfacial electron transfer from TiO_2 to Pt NPs via MoS_2. Additionally, PMSTB shows a relatively broader PL spectrum indicating the contribution from the hydroxyl group attached to the TiO_2 surface, which is consistent with the XPS analysis.

View Article Online
DOI: 10.1039/C8TA06783J

3.4. Hydrogen evolution reaction (HER) study

The visible light HER performance of various catalysts, such as TB, MS, MSTB, PMS, PTB and PMSTB as working electrodes made on glassy carbon disk was investigated in an N_2-saturated 0.5M H_2SO_4 solution using a typical three-electrode linear sweep voltammetry (LSV) method. For a better comparison, each measurement has been repeated under dark conditions as well. The electrochemical HER activities (LSVs) of various catalysts under dark and light (wavelength range 370-730 nm) are shown in Fig. 8(a,b) and the corresponding Tafel slopes are shown in Fig. 8(c,d), respectively. Note that the our results are nearly independent of scan rates in the range 2-10 mV/s (see Fig. S9 and Table S1, Supporting Information) and the presented data corresponds to a scan rate of 5mV/s. As shown in Fig. 8(a), the HER for pristine TiO_2 NBs starts at a potential of –623 mV and –616 mV (versus RHE) under dark and light, respectively, above which the current increases drastically. In spite of very low overall current density, TB presents a HER overpotential (to attain –10 mA/cm^2 current density) of –796 mV under light at a current density of 10 mA/cm^2, which is positively shifted by 87 mV as compared to that under dark. The pristine few-layer MoS_2 exhibits much enhanced current density with low onset potential of –246 mV, which reduces to –193 mV after light illumination. The overpotential is observed to be –425 mV and –395 mV under dark and light, respectively (see Table 2). Interestingly, in MSTB the uniform decoration of edge-exposed few-layer MoS_2 on the porous sites of TiO_2 NBs decreases the onset potential to –215 mV in dark, which further reduces to –178 mV after irradiation with visible light as compared to that of bare TiO_2 and MoS_2 nanostructures. In MSTB, the overpotentials are calculated to be –336 mV and –305 mV under dark and light conditions, respectively. Thus, it can be concluded that more carriers are being generated in MSTB with light irradiation, which augments the reduction process of electroadsorbed protons. The introduction of merely ~1.4 wt% Pt NP on the TB, MS, and MSTB results in a

View Article Online
DOI: 10.1039/C8TA06783J

dramatic reduction in the onset potential towards HER reaction. For PMS, it is measured to be –76 mV and –66 mV, while for PTB it is observed at –45 mV and –41 mV, under dark and light, respectively. In case of PMSTB, onset potential under dark is measured to be –40 mV, which is dramatically reduced to –9 mV after light irradiation, which essentially outperforms the commercial Pt/C electrode (–48 mV) with much higher Pt content. The summary of the performance of various catalysts is presented in Table 2. As evident from the table, the PMSTB exhibits exceptionally low overpotential under the light, –74 mV, which is much lower (by 23 mV) than the value measured in dark (–97 mV) and this is further lower than the commercial Pt/C electrode (–106 mV). Thus, a dramatic enhancement in the photogenerated charge carriers, as well as reduced charge transfer resistance, is expected in the systems after the Pt NP decoration, which serves as favorable nodes with large electron-accepting and buffering properties to facilitate electron transport, which in turn improve the overall conductivity.[4]

Tafel slopes of all the samples in both dark and light (in mV decade^{-1}), estimated from the linear fit of overpotential and logarithmic function of current density (log|j|), are shown in Fig. 8(c,d) and tabulated in Table 2. Lower Tafel slopes not only reveal about the rate-determining step of the hydrogen evolution electrocatalysis mechanism but are also desirable to minimize the energy input required to achieve a targeted HER current density. From Fig. 8(c, d), it is evident that in each catalyst the Tafel slope decreases after the illumination of light compared to their respective dark values, which eventually confirms the acceleration of the electron transfer kinetics upon irradiation. In dark, a much lower Tafel slope is estimated for pristine MS (119 mV dec^{-1}) than for pristine TB (170 mV dec^{-1}), which further decreases in their composite system (MSTB) to 112 mV dec^{-1}. Under visible light illumination, their corresponding values are calculated to be 135 mV dec^{-1} (TB), 107 mV dec^{-1} (MS) and 92 mV dec^{-1} (MSTB), as shown in Table 2. After Pt NP loading on MS, TB, and MSTB, the Tafel

View Article Online
DOI: 10.1039/C8TA06783J

slope is observed to be decreased drastically, as demonstrated in Fig. 8(d). Tafel slopes for PMS and PTB are 59 and 53 mV dec^{-1} under dark, and 56 and 50 mV dec^{-1} under the light, respectively. PMSTB exhibits exceptionally low Tafel slope (30 mV dec^{-1}) under the light, which is much lower (19 mV dec^{-1}) than the value measured under dark (49 mV dec^{-1}) and our values are comparable/ better than that of a commercial Pt/C electrode (32 mV dec^{-1}). Two main reaction pathways are widely accepted in HER electrocatalysis, commencing with a primary discharge step (i.e., Volmer reaction: $H_3O^+ + e^- \rightarrow H_{adsorbed}$), followed by either the electrochemical desorption step (i.e., Heyrovsky reaction: $H_3O^+ + e^- + H_{adsorbed} \rightarrow H_2$) or the monoatomic hydrogen recombination step (i.e., Tafel reaction: $H_{adsorbed} + H_{adsorbed} \rightarrow H_2$). As broadly reported in the literature, Tafel slopes of ~120 mV dec^{-1}, ~40 mV dec^{-1}, and ~30 mV dec^{-1} are allocated to Volmer, Heyrovsky and Tafel reactions being the HER rate-determining step, respectively.[60, 61]. In our case, the Tafel slopes of all the HSs photocatalysts (MSTB, PMS, PTB, and PMSTB) fall between the Volmer mechanism and the Tafel mechanism indicating that the Volmer−Tafel mechanism plays the predominant role in the catalysts' HER kinetics.[62] The lowest Tafel slope found for PMSTB under visible light illumination (i.e. enhanced HER kinetics) consequently supports its high HER performance.

Electrochemical impedance spectroscopy (EIS) is a powerful technique to characterize interface reactions and heterogeneous electron transfer process in HER.[63] Fig. 9(a-d) and Fig. S7(a, b) (Supporting Information) show the Nyquist plots of all the samples corresponding to their EIS response. The charge transfer resistance (R_{ct}) values have been calculated for all the samples estimated from the Randles circuit (see Fig. S7(c), Supporting Information) under dark and light condition[64]. In dark, the R_{ct} is calculated to be lower for MSTB (102 Ω) as compared to the pristine TB (527 Ω) as well as MS (132 Ω). Interestingly, after the Pt NP decoration, the R_{ct} dramatically reduces to 36 Ω, 33 Ω and 27 Ω for PMS,

View Article Online
DOI: 10.1039/C8TA06783J

PTB, and PMSTB, respectively, under dark. The R_{ct} values of all catalysts are decreased even further upon illumination, indicating the presence of photogenerated carriers in these electrodes, as tabulated in Table 2 and Fig. 9(e). Under illumination, R_{ct} for PMSTB decreases to the minimum value of 14 Ω indicating the augmented charge transfer process in the presence of light. The heavy n-type doping in the catalytically-active edge-exposed MoS_2 NFs (as demonstrated from Raman analysis, see Fig. 4(c)) provides a fast electron transfer from TiO_2 side to the MoS_2 side and results in a superior HER kinetics, which is dramatically enhanced after the introduction of metallic and highly-active catalyst Pt NP into the MSTB system.

Further insight into the HER electrocatalysts intrinsic activity can be obtained by comparison of exchange current density (j_0) values, which is determined by the ability to exchange electrons from the working electrode to the counter electrode through the electrolyte solution at null potential. Fig. 9(f) compiles exchange current density, j_0, values obtained under dark and light conditions for all studied samples. It is noteworthy that a dramatic enhancement (~10-fold) in j_0 value is observed in TB under visible light after the decoration with MoS_2 layers. Furthermore, for all samples tested, there is a significant increase in j_0 values after visible light illumination, consistent with the lower R_{ct} and Tafel slope values found after light irradiation. Among the various electrodes studied here, PMSTB showed the highest j_0 (~0.182 mA/cm^2 under dark and 0.296 mA/cm^2 under visible light). Thus, the aforementioned enhanced HER performance of MSTB is a result of the efficient charge transport and favorable HER kinetics at the interface of the HS components, which is further enhanced after decoration with Pt NP, widely regarded as the best performing noble metal catalyst for the HER.

To evaluate the durability of as-prepared catalyst, the cyclic durability, as well as long term stability, was investigated, and the results are presented in Fig. 10(a). Long-term cycling

View Article Online
DOI: 10.1039/C8TA06783J

experiment (up to 22 hours) was performed for PMSTB by recording 10,000 cycles from 0 V to -0.2 V vs. RHE. As shown in Fig. 10(a), the polarization curve shows no loss in current density after 10,000 CV cycles, though the performance marginally improves with time, which may be due to the improved interfacial contact and possible Pt dissolution/ redeposition at the PMSTB surface, which may yield an increase in the HER active sites. The long term stability test was performed by chronopotentiometry measurements to evaluate the catalyst capability of sustaining a 10 mA/cm^2 cathodic current over a 12 hr period (see inset of Fig. 10(a)). The catalyst PTB shows the initial decay of HER performance up to 3 hr of operation (-0.270 V @ 3 hr vs. -0.123 V @ 0 hr), indicating the stabilization of the anchoring effect of MoS_2 with respect to the decorated Pt NPs. Beyond 3 hr, PTB performance marginally improves up with time up to 12 hr (-0.238 V @ 3 hr). PMSTB shows a similar trend with an initial decay of HER performance with time up to 3 hr, as shown in the inset of Fig. 10(a). Eventually, it reaches HER performance of -0.195 V @ 12 hr, which is better than PTB. Note that after 12 hr of continuous galvanostatic operation at 10 mA/cm^2, the HER performance of PMSTB decays by ~90 mV. Additionally, some intermittent fluctuation in the potential values is observed for PMSTB beyond ~4 hr of continuous operation, which may be due to the mild oxidation of the MoS_2 sites accelerated by the anchored Pt NPs and the H_2 bubble movement. We cannot rule out the effect of leaching of the samples in MoS_2 and Pt-based ternary systems, which necessitates a more careful sample preparation for such experiments. Interestingly, the performance of MSTB initially improves with time and then reaches a saturation value. Possible coarsening of the MoS_2 layer along with electrochemical activation of the high binding energy S_2^{2-} sites upon irreversible HER cathodic cleaving may explain the observed enhancement[55, 65]. To understand the structural stability of the catalyst, the Raman spectra of MSTB were recorded before and after the PEC reaction. The crystallinity and stability of both TiO_2(B) and MoS_2 components are observed to be retained

View Article Online
DOI: 10.1039/C8TA06783J

under the PEC reaction, as evident from Fig. S6 (Supporting Information). However, the relative intensity of MoS_2 characteristic peaks slightly decreases after the reaction, which may be due to oxidation and associated introduction of defects in the MoS_2 layers. One additional Raman peak is detected at ~820 cm^{-1} after the PEC reaction, which may be assigned to the M=O bond[66, 67] resulting from the marginal oxidation of MoS_2 in the acidic media. However, chronopotentiometric measurement shows that the MSTB catalyst exhibits excellent stability towards HER activity up to 12 hr, confirming the non-photocorrosive nature of our catalyst.

We believe that the interplay between Pt and MoS_2 interfaces, which ultimately results in enhanced HER performances, is not just the synergistic effect of Pt promotion of initially inactive MoS_2 sites and reduction in the TiO_2 bandgap, but also the mechanical anchoring provided by MoS_2 and the inherently high Pt HER electroactivity and conductivity. In addition, appropriate band bending at the multiple interfaces sweeps away the charge carriers and allow them to participate in the enhanced HER activity.

3.5. Mechanism of enhanced HER activity

Though MoS_2 is known as a catalytically active material, poor charge transport in the basal plane is often responsible for it inferior HER performance. Fabrication of edge-exposed MoS_2 and activation of the inert basal plane through Pt doping or extrinsic S vacancy generation have proven to be successful strategies to trigger superior HER electrocatalytic activities.[68-70] In this study, few-layer MoS_2 with a high density of catalytically-active edge-exposed sites are tightly coupled with the porous surface of S-doped TiO_2 NBs. Structural analysis by HRTEM and STEM imaging of the as-grown MoS_2 layers on the TiO_2 NBs confirms their edge-rich nature, and presence of surface defects. This defect-rich structure leads to a higher exposure of unsaturated sulfur edge sites, which are widely regarded as the active sites responsible for the overall HER activity.[22, 55] Additionally, the MoS_2 layers grown

View Article Online
DOI: 10.1039/C8TA06783J

onto the TiO_2 NBs surface present an n-type doping of MoS_2, contributing to maximize HER activities after MoS_2 basal plane activation.

Upon illumination with visible light, electrons in TiO_2, as well as MoS_2 in the HSs, may be excited, as confirmed by the UV-visible absorption analysis. Due to the appropriate band alignment at the interface, the photogenerated electrons at the TiO_2 NBs can easily be transferred to the MoS_2 layer, avoiding possible recombination loss of carriers and it induces n-doping of the MoS_2 layer, as depicted in Fig. 10(b). The photo action spectra of different samples are shown in Fig. S8, confirming the visible light activation of electron-hole pairs and their efficient separation. Consequently, this efficient charge transfer occurring at the heterojunction (MSTB) greatly reduces the charge transfer resistance under visible light (88 Ω) and accounts for the enhanced exchange current density (j_0) under illumination, which is measured to be 0.019 mA/cm^2. A marginal amount of Pt NP (1.4 wt.%) loading on the MSTB is found to decorate the catalytically-active edge sites of MoS_2 as well as porous sites of TiO_2 with Pt NPs. The enhanced HER activities obtained after Pt decoration onto porous MoS_2 NFs/TiO_2 NBs indicate an even higher density of proton-accepting sites compared to MoS_2 NFs/TiO_2 NBs, which presumably arises from further activation of initially electrocatalytically-inert MoS_2 basal planes and S-edge sites. In addition, the presence of Pt NPs can also serve as advantageous metallic current collector nodes to facilitate lower resistance transport pathways of photo-excited electrons from TiO_2 domains to Pt NPs through MoS_2 (see Fig. 10(b)), improving the overall conductivity.[4] Hence, significantly enhanced HER activity was observed by PMSTB with a minimum charge transfer resistance of 14 Ω and a maximum exchange current density of 0.296 mA/cm^2. Additionally, the modification by H_2SO_4 decreases the work function of TiO_2, which changes its conduction band offset.[71] A schematic illustration of the excitation of electrons and their separation through two interfaces under the light irradiation is shown in Fig. 10(b) and this results in the

View Article Online
DOI: 10.1039/C8TA06783J

superior HER performance of the composite system. The structural defects and porous S-doped TiO_2 surface also promotes a closer interaction between MoS_2 and TiO_2 during solvothermal synthesis (i.e. higher availability of nucleation sites), which may be responsible for the catalytically active n-type doped structure of MoS_2 NFs. The detection of hydrogen gas during the electrocatalysis experiment and its quantification was made by the gas chromatography measurement and the results are presented in Fig. S10 and Fig. S11, respectively (supporting information).

On a separate note, the adsorbed hydroxyl group in TiO_2 lattice increases greatly after the decoration of MoS_2 layers (32.7%), which further enhances to 47.3% after the loading of Pt NPs on MSTB, as confirmed from XPS analysis. As the Volmer-Tafel HER mechanism is governing the HER performance in our HS catalysts, the higher presence of hydroxyl groups at the PMSTB electrode, known to facilitate electroadsorbed hydrogen desorption, may promote the rate-limiting electrochemical desorption step involving hydrogen gas formation.

Conclusion:

In summary, the hierarchical Pt@MoS_2/TiO_2 HS has been successfully grown via a three-step chemical process, which consists of solvothermal fabrication of TiO_2(B) NBs, its surface decoration by discrete few-layer MoS_2 by hydrothermal method followed by an in-situ decoration of Pt NPs onto it. Uniform decoration of MoS_2 layers on the porous sites of TiO_2 as well as a preferential decoration of Pt NPs on edge-sites/defect-sites of MoS_2 and porous sites of TiO_2 NBs has been evidenced by the FETEM and STEM analyses. The maximally edge-exposed MoS_2 NFs grown on and supported by the porous TiO_2 platform exhibits overall reduced layer numbers compared to the pristine MoS_2 layers and the MoS_2 NFs likely to be n-type doped, as revealed from the Raman analysis. In the HSs, MoS_2 exhibits exposed edge-sites, considered as the active nodes towards HER. The formation of

View Article Online
DOI: 10.1039/C8TA06783J

O_V rich MSTB and PMSTB with extremely high and broad visible to NIR absorption have been evidenced by the XPS and UV-visible absorption spectra, respectively. XPS analysis shows that the catalytically active bridging S_2^{2-}/apical S^{2-} increases up to ~72% after the formation of the ternary system, PMSTB. Formation of the well-coupled heterojunction between MoS_2 and S-doped TiO_2 accelerates the charge transfer rate from TiO_2 to MoS_2 side through the interfaces. Interestingly, Pt NPs anchored with the edge-sites of MoS_2 and porous sites of TiO_2 collect the photo-excited carriers making the HSs superior for HER activity than its individual counterparts. Under visible light illumination, the onset potential of MSTB is observed to be much lower (–178 mV) than that of TiO_2 (–616 mV) and MoS_2 (–193 mV) layer, with significant enhancement in the exchange current density. With the loading of 1.4 wt% Pt NP on MSTB, the onset potential, and the corresponding Tafel slope are reduced drastically to -9 mV and 30 mV dec^{-1}, respectively, with dramatically improved exchange current density (0.296 mA/cm^2). The Pt NP-supported HSs exhibit a giant enhancement in HER activity as evidenced by the EIS spectra. The presence of edge-defect enriched few-layer MoS_2 NFs on porous TiO_2 NBs, supported by the marginal amount of Pt NP exhibit extremely high hydrogen generation with high-performance stability at the working electrode through the Volmer-Tafel mechanism. Our results are very significant for the development of multicomponent catalysts

Acknowledgments

We acknowledge the financial support from MEITY (Grant No. 5(9)/2012-NANO(VOL-II)) for carrying out part of this work. N. Sreekanth acknowledges postdoctoral fellowship from SERB-NPDF (PDF/2016/002763), India. RKB acknowledges Marie-Sklowdowska-Curie individual fellowship under EU H2020 Programme (H2020-IF-2017; Grant No: 750929). D.E-L and N. V. R. thank the EPSRC for support through funding for the Centre for

View Article Online
DOI: 10.1039/C8TA06783J

Doctoral Training in Fuel Cells and their Fuels (EP/G037116/1, EP/L015749/1). A. J. P. thanks the EPSRC for support through funding for the School of Physics and Astronomy (EP/N509590/1). Central Instruments Facility, I.I.T. Guwahati is acknowledged for providing the Raman, TEM, and FESEM facilities. We thank Prof. M. Fujii, Kobe University, Japan for help in the XPS measurement. We are thankful to Prof. M. Qureshi, Anindya S. Patra, Gaurangi Gogoi and Tushar Kanta Sahu for their help in PEC experiments.

References:

1. C. G. Morales-Guio, L.-A. Stern and X. Hu, *Chem. Soc. Rev.*, 2014, **43**, 6555-6569.
2. H. Li, Y. Zhou, W. Tu, J. Ye and Z. Zou, *Adv. Funct. Mater.*, 2015, **25**, 998-1013.
3. Y. Lu, X. Cheng, G. Tian, H. Zhao, L. He, J. Hu, S.-M. Wu, Y. Dong, G.-G. Chang, S. Lenaerts, S. Siffert, G. Van Tendeloo, Z.-F. Li, L.-L. Xu, X.-Y. Yang and B.-L. Su, *Nano Energy*, 2018, **47**, 8-17.
4. X. Y. Xu, X. F. Dong, Z. J. Bao, R. Wang, J. G. Hu and H. B. Zeng, *J. Mater. Chem. A*, 2017, **5**, 22654-22661.
5. W. Zhou, W. Li, J.-Q. Wang, Y. Qu, Y. Yang, Y. Xie, K. Zhang, L. Wang, H. Fu and D. Zhao, *J. Am. Chem. Soc.*, 2014, **136**, 9280-9283.
6. W. Zhou, F. Sun, K. Pan, G. Tian, B. Jiang, Z. Ren, C. Tian and H. Fu, *Adv. Funct. Mater.*, 2011, **21**, 1922-1930.
7. Y.-P. Yuan, L.-W. Ruan, J. Barber, S. C. Joachim Loo and C. Xue, *Energy Environ. Sci.*, 2014, **7**, 3934-3951.
8. Y. Gai, J. Li, S.-S. Li, J.-B. Xia and S.-H. Wei, *Phys. Rev. Lett*, 2009, **102**, 036402.
9. W. J. Zhou, Y. H. Leng, D. M. Hou, H. D. Li, L. G. Li, G. Q. Li, H. Liu and S. W. Chen, *Nanoscale*, 2014, **6**, 4698.
10. W. Zhou and H. Fu, *ChemCatChem*, 2013, **5**, 885-894.
11. K. K. Paul, S. Jana and P. K. Giri, *Part. Part. Syst. Char.*, 2018, **35**, 1800198.
12. K. K. Paul, R. Ghosh and P. K. Giri, *Nanotechnology*, 2016, **27**, 315703.
13. K. K. Paul and P. K. Giri, in *Reference Module in Chemistry, Molecular Sciences and Chemical Engineering*, Elsevier, 2017, DOI: https://doi.org/10.1016/B978-0-12-409547-2.13176-2.
14. K. K. Paul and P. K. Giri, *J. Phys. Chem. C*, 2017, **121**, 20016-20030.
15. M.-Z. Ge, C.-Y. Cao, S.-H. Li, Y.-X. Tang, L.-N. Wang, N. Qi, J.-Y. Huang, K.-Q. Zhang, S. S. Al-Deyab and Y.-K. Lai, *Nanoscale*, 2016, **8**, 5226-5234.
16. A. Tanaka, A. Ogino, M. Iwaki, K. Hashimoto, A. Ohnuma, F. Amano, B. Ohtani and H. Kominami, *Langmuir*, 2012, **28**, 13105.
17. M. A. Khan, L. Sinatra, M. Oufi, O. M. Bakr and H. Idriss, *Catal. Lett.*, 2017, **147**, 811-820.
18. K. K. Paul and P. K. Giri, *J. Nanosci. Nanotechnol.*, 2019, **19**, 307-331.
19. F.-X. Xiao, S.-F. Hung, H. B. Tao, J. Miao, H. B. Yang and B. Liu, *Nanoscale*, 2014, **6**, 14950-14961.
20. J. Greeley, T. F. Jaramillo, J. Bonde, I. Chorkendorff and J. K. Nørskov, *Nat. Mater.*, 2006, **5**, 909.
21. S. Stankovich, D. A. Dikin, G. H. B. Dommett, K. M. Kohlhaas, E. J. Zimney, E. A. Stach, R. D. Piner, S. T. Nguyen and R. S. Ruoff, *Nature*, 2006, **442**, 282-286.

View Article Online
DOI: 10.1039/C8TA06783J

22. D. Escalera-López, Y. Niu, S. J. Park, M. Isaacs, K. Wilson, R. E. Palmer and N. V. Rees, *Appl. Catal. B Environ.*, 2018, **235**, 84-91.
23. C. Liu, L. Wang, Y. Tang, S. Luo, Y. Liu, S. Zhang, Y. Zeng and Y. Xu, *Appl. Catal. B Environ.*, 2015, **164**, 1-9.
24. Y. Dong, S.-Y. Chen, Y. Lu, Y.-X. Xiao, J. Hu, S.-M. Wu, Z. Deng, G. Tian, G.-G. Chang, J. Li, S. Lenaerts, C. Janiak, X.-Y. Yang and B.-L. Su, *Chem Asian J.*, 2018, **13**, 1609-1615.
25. Y. Kim, D. H. K. Jackson, D. Lee, M. Choi, T.-W. Kim, S.-Y. Jeong, H.-J. Chae, H. W. Kim, N. Park, H. Chang, T. F. Kuech and H. J. Kim, *Adv. Funct. Mater.*, 2017, **27**, 1701825.
26. B. Chen, E. Liu, T. Cao, F. He, C. Shi, C. He, L. Ma, Q. Li, J. Li and N. Zhao, *Nano Energy*, 2017, **33**, 247-256.
27. Y. Pi, Z. Li, D. Xu, J. Liu, Y. Li, F. Zhang, G. Zhang, W. Peng and X. Fan, *ACS Sustain. Chem. Eng.*, 2017, **5**, 5175-5182.
28. H. Li, Y. Wang, G. Chen, Y. Sang, H. Jiang, J. He, X. Li and H. Liu, *Nanoscale*, 2016, **8**, 6101-6109.
29. Y. Li, Y.-L. Li, C. M. Araujo, W. Luo and R. Ahuja, *Catal. Sci. Technol.*, 2013, **3**, 2214-2220.
30. D. Wang, Z. Wang, C. Wang, P. Zhou, Z. Wu and Z. Liu, *Electrochem commun.*, 2013, **34**, 219-222.
31. K. Y. Honglin Li, Chao Li, Zheng Tang, Bangjun Guo, Xiang Lei, Hao Fu & Ziqiang Zhu, *Scientific Reports*, 2015, **5**, 18730.
32. D. Voiry, M. Salehi, R. Silva, T. Fujita, M. Chen, T. Asefa, V. B. Shenoy, G. Eda and M. Chhowalla, *Nano Lett.*, 2013, **13**, 6222-6227.
33. M. A. Lukowski, A. S. Daniel, F. Meng, A. Forticaux, L. Li and S. Jin, *J. Am. Chem. Soc.*, 2013, **135**, 10274-10277.
34. J. Xie, H. Zhang, S. Li, R. Wang, X. Sun, M. Zhou, J. Zhou, X. W. Lou and Y. Xie, *Adv. Mater.*, 2013, **25**, 5807-5813.
35. D. Escalera-López, Y. Niu, J. Yin, K. Cooke, N. V. Rees and R. E. Palmer, *ACS Catal.*, 2016, **6**, 6008-6017.
36. H. Li, C. Tsai, A. L. Koh, L. Cai, A. W. Contryman, A. H. Fragapane, J. Zhao, H. S. Han, H. C. Manoharan, F. Abild-Pedersen, J. K. Nørskov and X. Zheng, *Nat. Mater.*, 2015, **15**, 48.
37. J. Xie, H. Zhang, S. Li, R. Wang, X. Sun, M. Zhou, J. Zhou, X. W. Lou and Y. Xie, *Adv. Mater.*, 2013, **25**, 5807-5813.
38. W. Zhou, Z. Yin, Y. Du, X. Huang, Z. Zeng, Z. Fan, H. Liu, J. Wang and H. Zhang, *Small*, 2013, **9**, 140-147.
39. H. Yu, X. Yu, Y. Chen, S. Zhang, P. Gao and C. Li, *Nanoscale*, 2015, **7**, 8731-8738.
40. N. Zhang, S. Gan, T. Wu, W. Ma, D. Han and L. Niu, *ACS Appl. Mater. Interfaces*, 2015, **7**, 12193-12202.
41. X. Chia, N. A. A. Sutrisnoh and M. Pumera, *ACS Appl. Mater. Interfaces*, 2018, **10**, 8702-8711.
42. C. E. Blackmore, N. V. Rees and R. E. Palmer, *Phys. Chem. Chem. Phys.*, 2015, **17**, 28005-28009.
43. E. Kemppainen, A. Bodin, B. Sebok, T. Pedersen, B. Seger, B. Mei, D. Bae, P. C. K. Vesborg, J. Halme, O. Hansen, P. D. Lund and I. Chorkendorff, *Energy Environ. Sci.*, 2015, **8**, 2991-2999.
44. S. Li, T. Pu, J. Wang, X. Fang, Y. Liu, S. Kang and L. Cui, *Int. J. Hydrog. Energy*, 2018, **43**, 16534-16542.
45. K. K. Paul, N. Sreekanth, R. K. Biroju, T. N. Narayanan and P. K. Giri, *Sol. Energy Mater Sol. Cells*, 2018, **185**, 364-374.
46. X.-Y. Yang, L.-H. Chen, Y. Li, J. C. Rooke, C. Sanchez and B.-L. Su, *Chem. Soc. Rev.*, 2017, **46**, 481-558.
47. N. Li, X. Zhang, W. Zhou, Z. Liu, G. Xie, Y. Wang and Y. Du, *Inorganic Chemistry Frontiers*, 2014, **1**, 521-525.
48. S.-H. Nam, T. K. Kim and J.-H. Boo, *Catalysis Today*, 2012, **185**, 259-262.
49. Z. Yin, Z. Zeng, J. Liu, Q. He, P. Chen and H. Zhang, *Small*, 2013, **9**, 727-731.

View Article Online
DOI: 10.1039/C8TA06783J

50. K. C. J. Lee, Y.-H. Chen, H.-Y. Lin, C.-C. Cheng, P.-Y. Chen, T.-Y. Wu, M.-H. Shih, K.-H. Wei, L.-J. Li and C.-W. Chang, *Sci. Rep.*, 2015, **5**, 16374.
51. D. Kiriya, M. Tosun, P. Zhao, J. S. Kang and A. Javey, *J. Am. Chem. Soc.*, 2014, **136**, 7853-7856.
52. A. Shaista, S. Arun Kumar and E. Jonghwa, *Sci. Technol. Adv. Mater*, 2015, **16**, 035009.
53. B. Yue, Y. Ma, H. Tao, L. Yu, G. Jian, X. Wang, X. Wang, Y. Lu and Z. Hu, *J. Mater. Chem.*, 2008, **18**, 1747-1750.
54. K. Yang, J. Li, Y. Peng and J. Lin, *Phys. Chem. Chem. Phys.*, 2017, **19**, 251-257.
55. L. R. L. Ting, Y. Deng, L. Ma, Y.-J. Zhang, A. A. Peterson and B. S. Yeo, *ACS Catal.*, 2016, **6**, 861-867.
56. B. Santara, P. K. Giri, K. Imakita and M. Fujii, *Nanoscale*, 2013, **5**, 5476.
57. W. Ho, J. C. Yu, J. Lin, J. Yu and P. Li, *Langmuir*, 2004, **20**, 5865-5869.
58. M. Cueto, M. Piedrahita, C. Caro, B. Martínez-Haya, M. Sanz, M. Oujja and M. Castillejo, *J. Phys. Chem. C*, 2014, **118**, 11432-11439.
59. S.-M. Wu, X.-L. Liu, X.-L. Lian, G. Tian, C. Janiak, Y.-X. Zhang, Y. Lu, H.-Z. Yu, J. Hu, H. Wei, H. Zhao, G.-G. Chang, G. Tendeloo, L.-Y. Wang, X.-Y. Yang and B.-L. Su, *Adv. Mater.*, 2018, **30**, 1802173.
60. D. Hou, W. Zhou, X. Liu, K. Zhou, J. Xie, G. Li and S. Chen, *Electrochim. Acta*, 2015, **166**, 26-31.
61. Y. Li, H. Wang, L. Xie, Y. Liang, G. Hong and H. Dai, *J. Am. Chem. Soc.*, 2011, **133**, 7296-7299.
62. B. Ma, P.-Y. Guan, Q.-Y. Li, M. Zhang and S.-Q. Zang, *ACS Appl. Mater. Interfaces*, 2016, **8**, 26794-26800.
63. L. Liao, J. Zhu, X. Bian, L. Zhu, M. D. Scanlon, H. H. Girault and B. Liu, *Adv. Funct. Mater.*, 2013, **23**, 5326-5333.
64. R. K. Biroju, S. Pal, R. Sharma, P. K. Giri and T. N. Narayanan, *Nanotechnology*, 2017, **28**, 085101.
65. Y. Deng, L. R. L. Ting, P. H. L. Neo, Y.-J. Zhang, A. A. Peterson and B. S. Yeo, *ACS Catal.*, 2016, **6**, 7790-7798.
66. H. Nan, Z. Wang, W. Wang, Z. Liang, Y. Lu, Q. Chen, D. He, P. Tan, F. Miao, X. Wang, J. Wang and Z. Ni, *ACS Nano*, 2014, **8**, 5738-5745.
67. L. P. L. Mawlong, K. K. Paul and P. K. Giri, *J. Phys. Chem. C*, 2018, **122**, 15017-15025.
68. J. Deng, H. Li, J. Xiao, Y. Tu, D. Deng, H. Yang, H. Tian, J. Li, P. Ren and X. Bao, *Energy Environ. Sci.*, 2015, **8**, 1594-1601.
69. J. Hong, Z. Hu, M. Probert, K. Li, D. Lv, X. Yang, L. Gu, N. Mao, Q. Feng, L. Xie, J. Zhang, D. Wu, Z. Zhang, C. Jin, W. Ji, X. Zhang, J. Yuan and Z. Zhang, *Nat Commun.*, 2015, **6**, 6293.
70. H. Li, C. Tsai, A. L. Koh, L. Cai, A. W. Contryman, A. H. Fragapane, J. Zhao, H. S. Han, H. C. Manoharan, F. Abild-Pedersen, J. K. Nørskov and X. Zheng, *Nat. Mater.*, 2015, **15**, 48.
71. X. Song, G. Chen, L. Guan, H. Zhang and J. Tao, *Appl. Phys. Express*, 2016, **9**, 095801.

View Article Online
DOI: 10.1039/C8TA06783J

Table Captions:

Table 1: Summary of the samples, their effective band gap, the relative percentage of oxygen vacancy (O_V), hydroxyl group (O_H), lower and higher binding energy (BE) S present in the samples.

Sample code	Sample	Various species from deconvoluted XPS spectra (in %)			
		O_V	O_H	Lower BE S (terminal and unsaturated)	Higher BE S (bridging and apical)
TB	TiO_2(B)	22.2	18.4	-	-
MS	MoS_2	-	-	60.9	39.1
MSTB	MoS_2/TiO_2	46.1	32.7	45.6	54.4
PMS	Pt@MoS_2	-	-	-	-
PTB	Pt@TiO_2	15.5	23.1	-	-
PMSTB	Pt@MoS_2/TiO_2	31.4	47.3	27.8	72.2

Table 2: Comparison of various catalytic parameters of different photocatalysts under dark and light.

Catalyst code	Onset potential (at -0.5 mA/cm^2) [(mV) V RHE]		Overpotential at -10 mA/cm^2 [(mV) V RHE]		Tafel slope (mV dec^{-1})		Charge transfer resistance, R_{ct} (Ω)		Exchange current density, j_0 (mA/cm^2)	
	dark	light	dark	light	dark	light	dark	light	dark	light
TB	-623	-616	-883	-796	170	135	527	450	0.001	0.002
MS	-246	-193	-425	-395	119	107	132	121	0.008	0.013
MSTB	-215	-178	-336	-305	112	92	102	88	0.012	0.019
PMS	-76	-66	-147	-140	59	56	36	31	0.164	0.193
PTB	-45	-41	-113	-105	53	50	33	27	0.175	0.209
PMSTB	-40	-9	-97	-74	49	30	27	14	0.182	0.296
Pt/C	-48	-	-106	-	32	-	6	-	0.305	-

View Article Online
DOI: 10.1039/C8TA06783J

FIGURES:

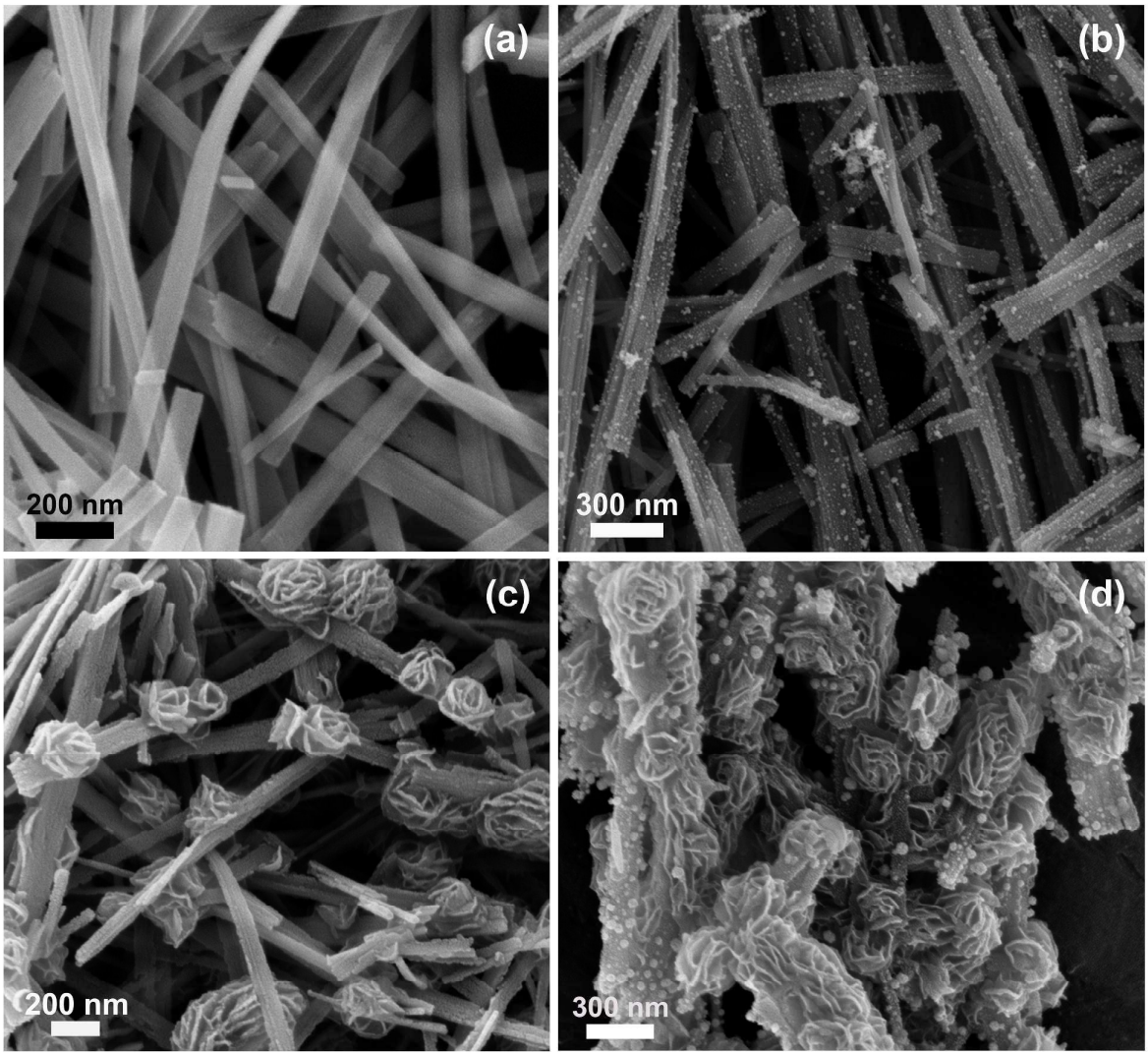

Fig. 1: FESEM images of (a) pristine TiO_2 NBs, (b) Pt NP decorated TiO_2 NBs, (c) MoS_2 NF decorated on TiO_2 NBs, and (d) Pt NP decorated MoS_2/TiO_2 HSs.

View Article Online
DOI: 10.1039/C8TA06783J

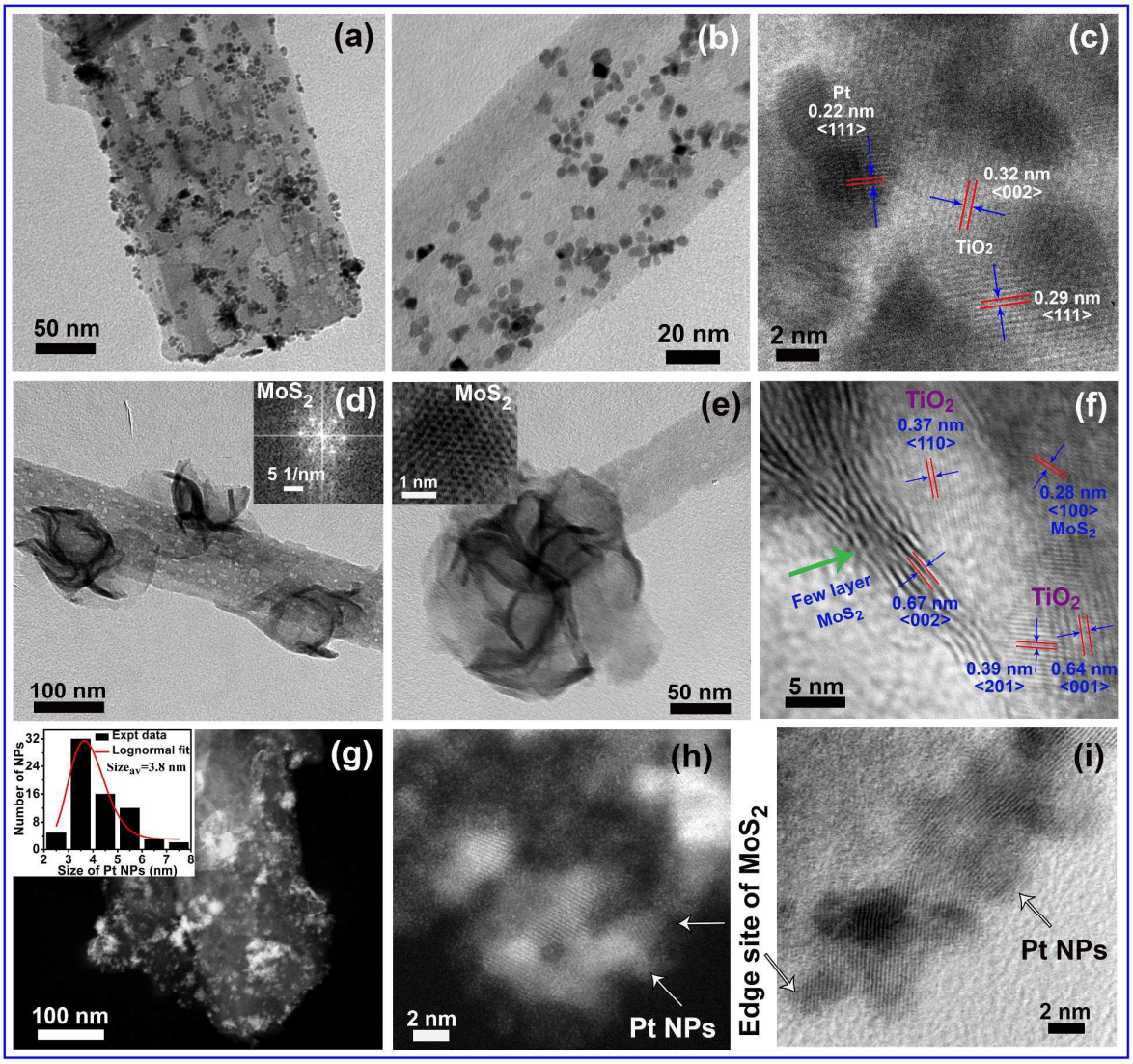

Fig. 2: (a, b) Pt NP decorated porous TiO_2 NBs at different magnifications, (c) HRTEM lattice fringe pattern showing the simultaneous presence of Pt and TiO_2. (d) TEM image of MoS_2 NF decorated nanoporous TiO_2 NB; inset shows the hexagonal diffraction spots on the NF site. (e) TEM image of TiO_2 NB coated with MoS_2 NF; the inset shows the BF-STEM image corresponding to the MoS_2 layer. (f) HRTEM lattice fringe pattern of MoS_2/TiO_2 HSs, (g) HAADF image of Pt NP decorated on MoS_2/TiO_2 HSs. Inset shows the size distribution of Pt NPs decorated on MoS_2/TiO_2 HSs. (h, i) High resolution dark field and bright field STEM images of Pt NPs selectively decorated on edge-sites of MoS_2 NF, respectively.

View Article Online
DOI: 10.1039/C8TA06783J

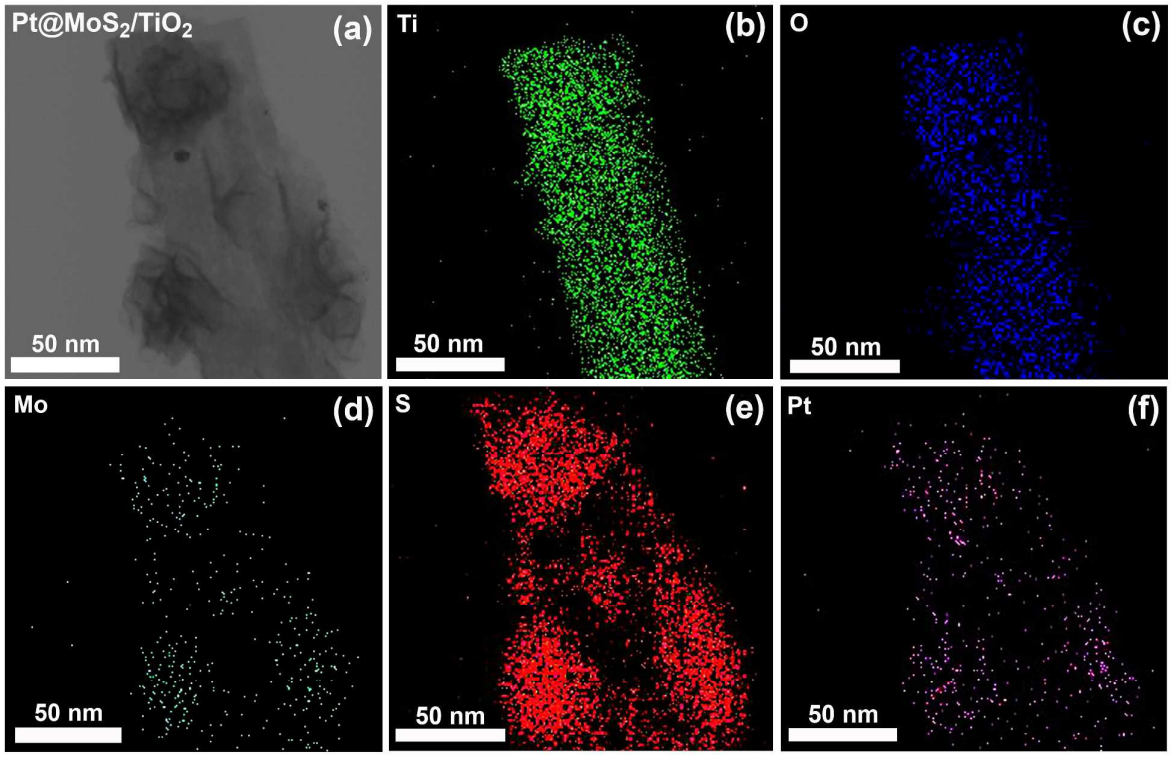

Fig. 3: STEM elemental mappings of PMSTB HS: (a) a raw image of the HS, (b-f) elemental maps of Ti, O, Mo, S and Pt, respectively.

View Article Online
DOI: 10.1039/C8TA06783J

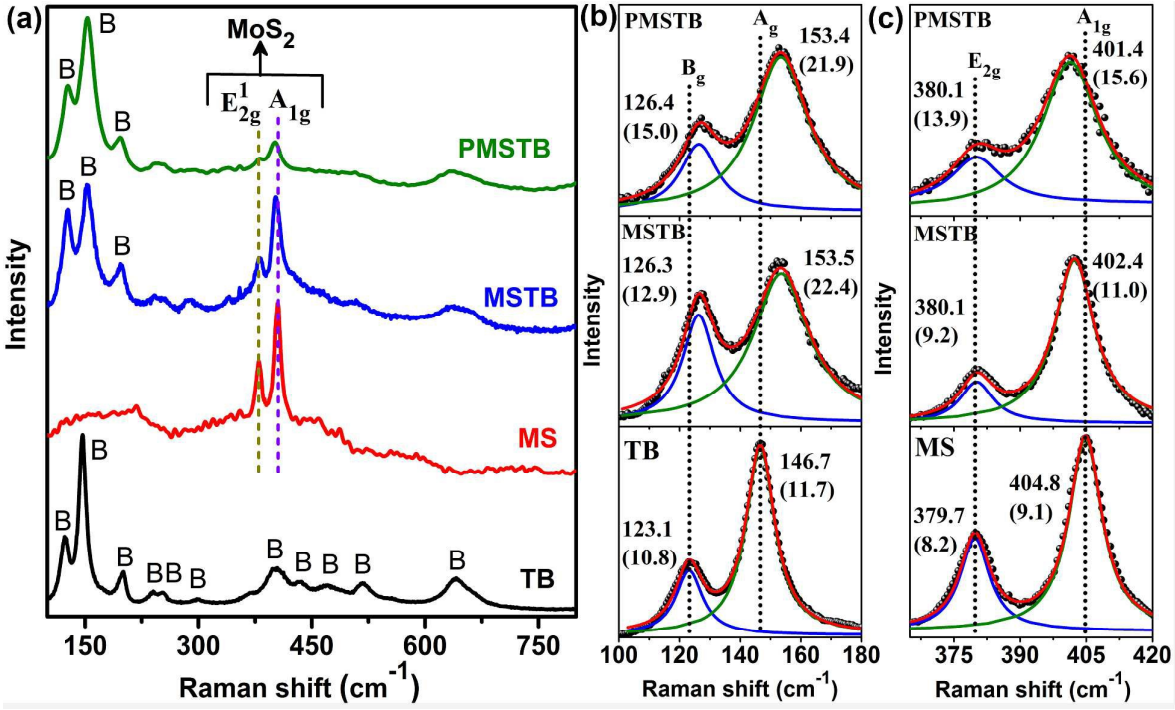

Fig. 4: (a) Raman spectra of pristine TiO_2(B) NBs, bare MoS_2 NFs, few-layer MoS_2 NFs decorated TiO_2(B) NBs and Pt loaded MoS_2/TiO_2 HSs. (b) Lorentzian fittings of Raman spectra for TB, MSTB and PMSTB in the range of 100-180 cm^{-1}. (c) Lorentzian fittings of active Raman modes of MoS_2 corresponding to the bare MoS_2, MSTB and PMSTB (360-420 cm^{-1}). The vertical dotted lines indicate the position of standard Raman mode of pristine MoS_2 and TiO_2(B).

View Article Online
DOI: 10.1039/C8TA06783J

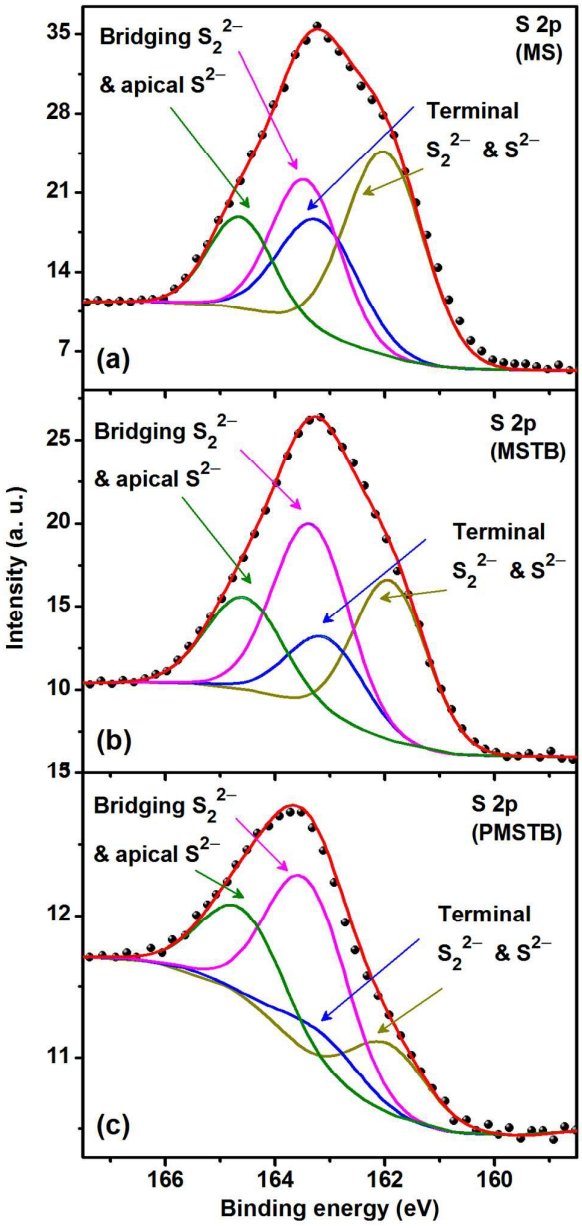

Fig. 5: S 2p core level XPS spectra for (a) MS, (b) MSTB and (c) PMSTB, fitted with the Shirley baseline. The symbols represent the experimental data and the solid lines correspond to the Gaussian fits. Identity of each fitted peak is denoted with corresponding charge states in the respective cases.

View Article Online
DOI: 10.1039/C8TA06783J

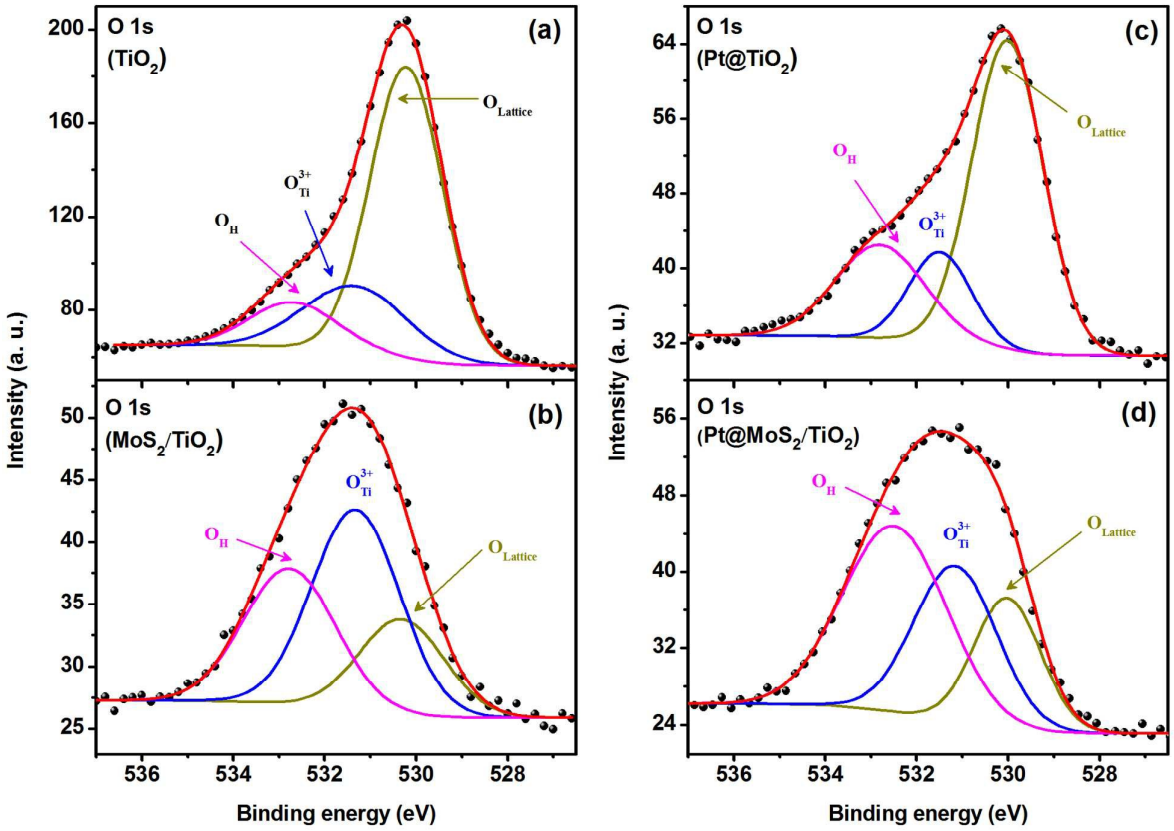

Fig. 6: O 1s core level XPS spectra of (a) TB, (b) MSTB, (c) PTB and (d) PMSTB with Gaussian fit of each spectrum with Shirley baseline. Symbols represent the experimental data and solid lines the Gaussian fits. Charge states associated with each peak is labeled in the spectrum.

View Article Online
DOI: 10.1039/C8TA06783J

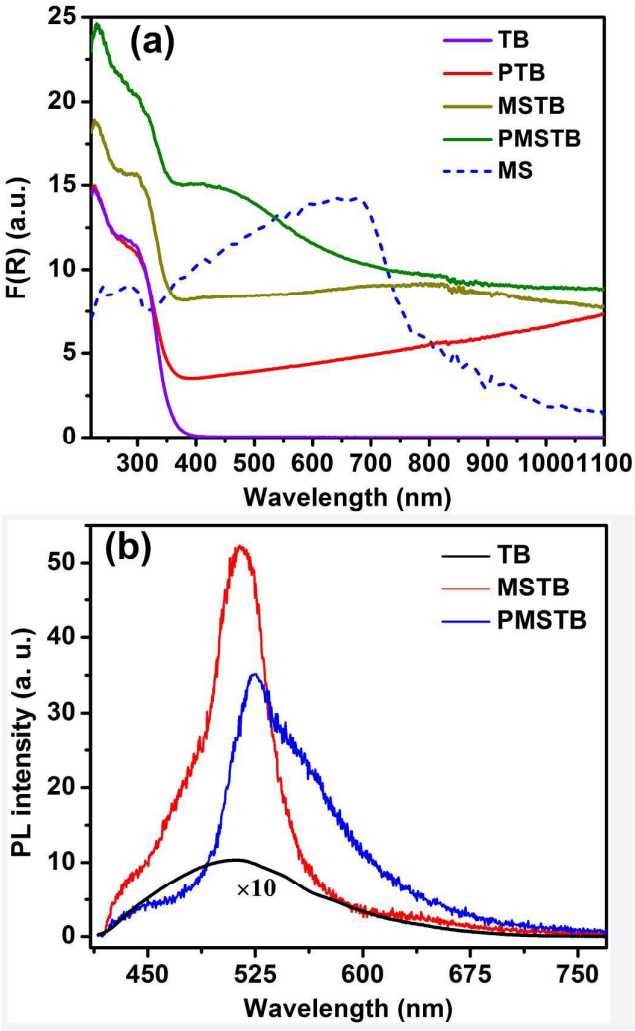

Fig. 7: (a) Kubelka–Munk plot, F(R), for different samples derived from the diffuse reflectance spectra. (b) PL spectra of TiO_2 and its HSs measured with 405 nm laser excitation. The PL spectrum of TB is shown in magnified scale to enable comparison.

View Article Online
DOI: 10.1039/C8TA06783J

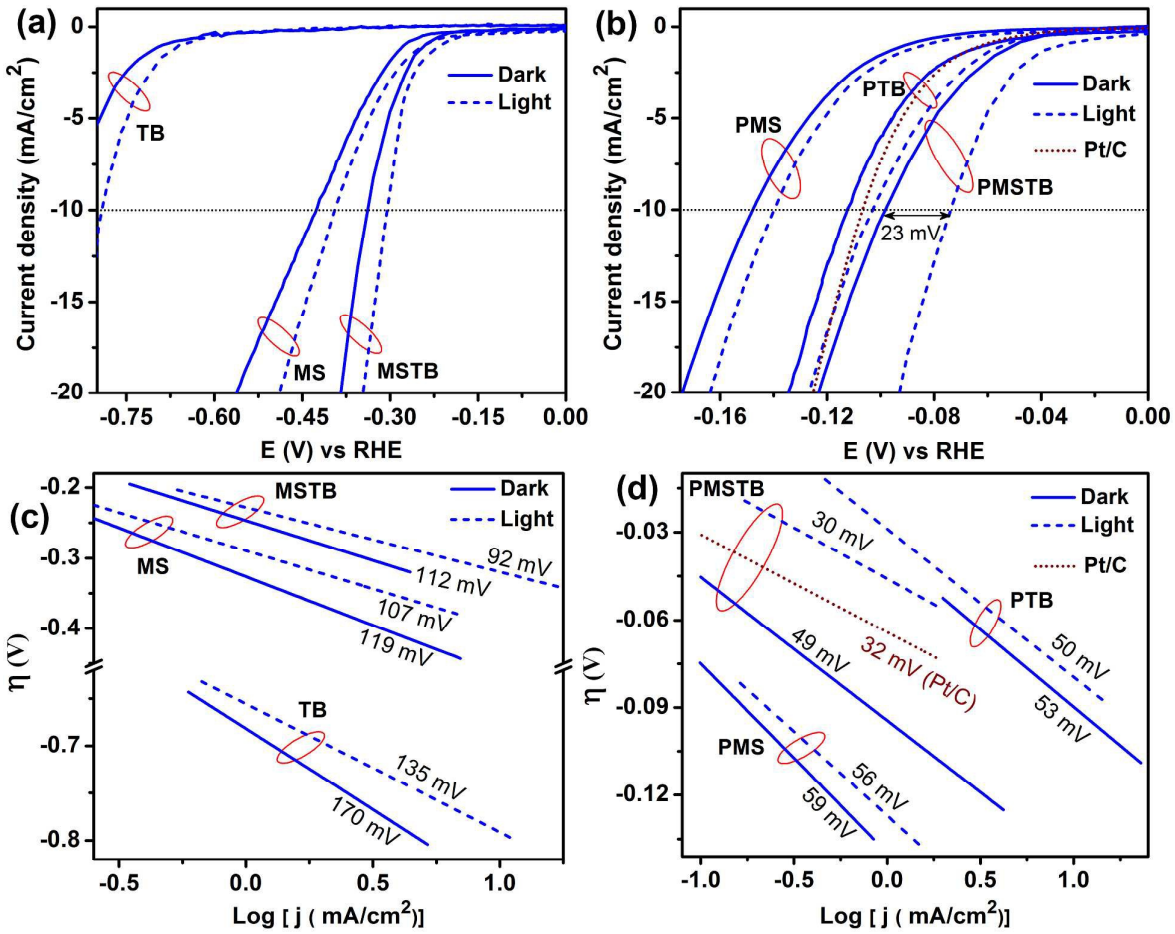

Fig. 8: Polarization curves of the hydrogen evolution reaction (HER) in dark and light conditions in (a) pristine TiO_2(B), MoS_2 and MoS_2/TiO_2(B) HS, (b) Pt@MoS_2, Pt@TiO_2 and Pt@MoS_2/TiO_2 HSs. (c, d) Tafel plots of different working electrodes derived from their LSV curves shown in (a,b), respectively. Polarization curve and the corresponding Tafel plot for Pt/C electrode are also shown in (b, d), respectively.

View Article Online
DOI: 10.1039/C8TA06783J

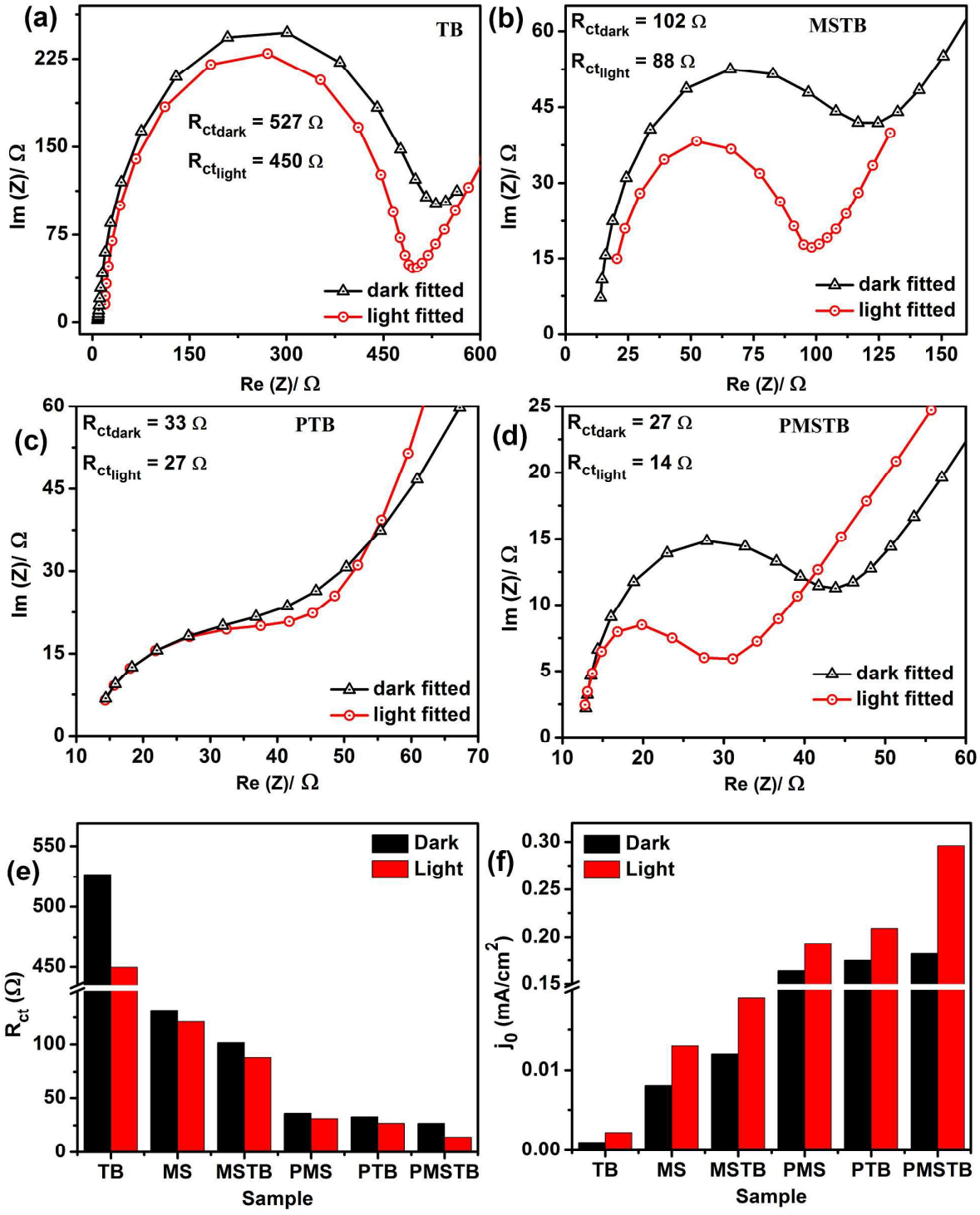

Fig. 9: Nyquist plots of (a) pristine TiO_2(B), (b) MoS_2/TiO_2, (c) Pt@TiO_2 and (d) Pt@MoS_2/TiO_2 HSs, under dark and light conditions. Note that the points represent experimental data, while the solid lines are simulation using the Randle's circuit to estimate the characteristic charge-transfer resistance (R_{ct}). (e, f) R_{ct} and j_0 values, respectively, of various electrodes in dark and light conditions.

View Article Online
DOI: 10.1039/C8TA06783J

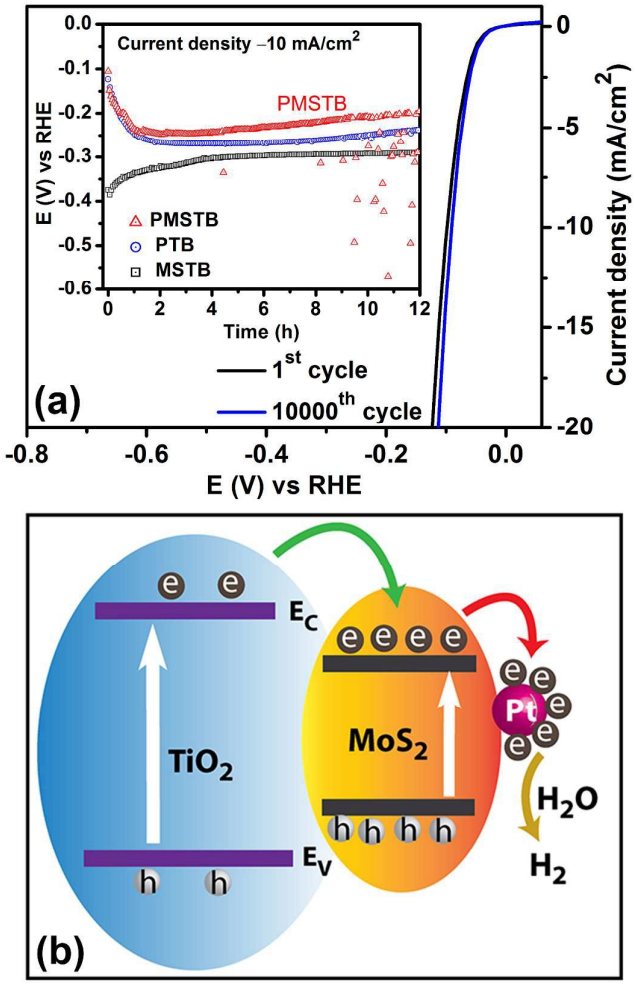

Fig. 10: (a) Polarization curves recorded for PMSTB before and after 10,000 CV cycles. Inset shows the chronopotentiometry showing the stability of the catalysts for 12 hr at a sustained current density of -10 mA/cm^2. (b) Schematic illustration of charge transfer at the multiple interfaces of PMSTB and the mechanism of enhanced visible light PEC activity of Pt NP decorated on TiO_2/MoS_2.

View Article Online
DOI: 10.1039/C8TA06783J

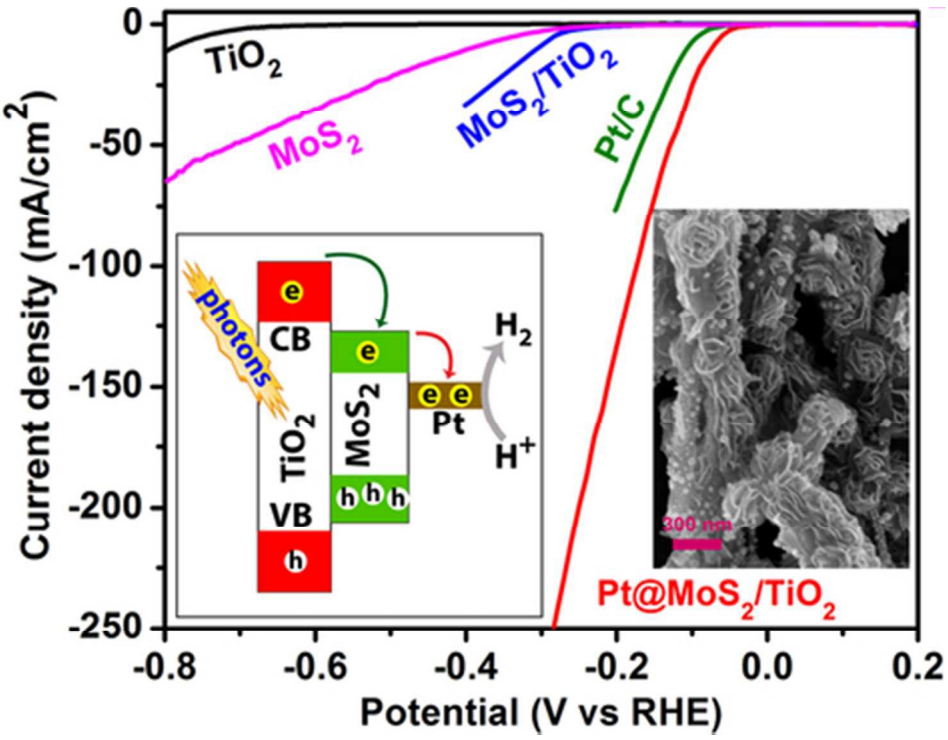

39x30mm (300 x 300 DPI)